UNIVERSITY OF ALBERTA

HOCHSCHULE FURTWANGEN UNIVERSITY HFU

MASTER-THESIS

Development of a Surgical Assistant System for Needle Adjustment in Prostate Brachytherapy

---

Field of Studies: Biomedical Engineering

Author:
Thomas Lehmann, B.Sc

Supervisors:
Prof. Dr.-Ing. Bernhard Vondenbusch
Mahdi Tavakoli, PhD

Villingen-Schwenningen
May 31, 2013

Kurzfassung

Titel der Master-Thesis

Entwicklung eines chirurgischen Asisstenzsystems für Nadelkorrektur in Prostata-Brachytherapie

---

Author: Thomas Lehmann
1. Betreuer: Prof. Dr.-Ing. Bernhard Vondenbusch, Hochschule Furtwangen University
2. Betreuer: Mahdi Tavakoli, PhD, University of Alberta
Semester: BME 3

Kurzfassung:

Der Prototyp eines chirurgischen Assistenzsystems wurde für das Prostata-Brachytherapie Verfahren entwickelt. Prostata-Brachytherapie is ein effektives, patientenfreundliches und minimal-invasives Krebs-Behandlungsverfahren. Die in dem Verfahren genutzten Nadeln weichen, bedingt durch ihre abgeschrägte Spitze, von ihrem angestebten Pfad ab. Die Ablenkung führt zu einer negativen Beeinflussung der Behandlungs-Effizienz und muss deshalb minimiert werden. Das entwickelte System ist der Prototyp eines intelligenten, chirurgischen Assistenz-Instruments mit zwei Freiheitsgraden. Der Hauptzweick des Systems ist die Vorhersage und Korrektur der Nadelspitzen-Ablenkung während dem Eingriff.

Für die Schätzung der Nadelablenkung in Echtzeit wurde ein auf einem Kraftsensor basierender virtueller Sensor entwickelt. Die an der Nadelbasis gemessenen Kraft- und Momentendaten werden von einem mathematischen Modell genutzt, das auf mechanische Eigenschaften der Nadel beruht. Das Modell schätzt die Ablenkung der Nadelspitze wärhend dem Einstich in Gewebe. Das Assistenzsystem ist dadurch in der Lage Ablenkungen in Echtzeit zu erkennen und Korrekturen vorzunehmen.

Die genutzte Methode für Abweichungskorrektur ist das Drehen der Nadel um 180° wenn ein vorbestimmter Schwellwert überschritten wurde, um den Effekt der Ablenkung umzukehren und die Nadel auf ihren gewünschten Pfad zurückzulenken.

Schlüsselwörter:

Medizinische Robotik, Brachytherapie, Abweichungskorrektur, Assistierte Chrirurgie

Abstract

Title of the Master-Thesis

Development of a Surgical Assistant System for Needle Adjustment in Prostate Brachytherapy

---

Author: Thomas Lehmann
1. Examiner: Prof. Dr.-Ing. Bernhard Vondenbusch, Hochschule Furtwangen University
2. Examiner: Mahdi Tavakoli, PhD, University of Alberta
Semester: BME 3

Abstract:

The prototype of a robotic surgical assistant system was developed for prostate brachytherapy. Prostate brachytherapy is an effective, patient friendly and minimally-invasive cancer treatment procedure. The needles, which are used in this procedure, deflect from the intended path due to their bevelled tip. This deflection leads to a negative influence on the treatment efficiency and should therefore be minimized. The developed system is the prototype of an intelligent, 2-DOF surgical assistant tool. The main purpose of the system is the prediction and correction of needle tip deflection during the procedure.

In order to estimate the needle deflection in real-time, a force sensor based virtual sensor was developed. The force sensor measures forces and moments at the needle base. The measured force/moment data is used by a mathematical model, which is based on mechanical needle properties. The model estimates the tip deflection of the needle in real-time during insertion into soft tissue. The assistant is therefore able to detect increasing deflection and carry out corrective measures in real-time.

The used method for deflection correction is turning the needle about 180° when a predetermined threshold is exceeded in order to reverse the effect of the bevel and bring the needle back to its desired path.

Keywords:

Medical robotics, brachytherapy, deflection correction, assisted surgery

Affirmation

I hereby declare on oath, that I have worked independently and without undue help from others to write this thesis.

The literary sources used are completely cited in the bibliography.

Schwenningen, May 31, 2013

Address: Thomas Lehmann
Hebelstraße 11
78144 Schramberg
Germany

Signature:

Acknowledgments

At this point I would like to express my sincerest thanks to my supervisors Prof. Dr.-Ing. Bernhard Vondenbusch, who is with the Hochschule Furtwangen University and Dr. Mahdi Tavakoli, who is with the University of Alberta for their support and advice. I would particularly like to thank Dr. Tavakoli for his ever-present support, motivation, encouragement, and sponsorship during my time at the University of Alberta and for providing me with the opportunity to engage in an interesting and rewarding research project.

Furthermore, I would like to thank the Department of Electrical and Computer Engineering of the University of Alberta for the sponsorship during my time in Edmonton and for the assistance in providing this research opportunity.

I would also like to thank Dr. Nawaid Usmani and Dr. Ronald Sloboda for their advice, feedback and time.

Many thanks to Herbert Dexel and the staff of the Department of Electrical and Computer Engineering's machine shop for their excellent work on the prototype setup and valuable feedback on the design of the setup.

Finally, thank you to my fellow students Ali Jazayeri, Arefeh Boroomand, Jian Li, Matthew Dyck, Meaghan Bowthorpe, Noushin Miandashti, Ran Tao and Victor Mendez of the Telerobotic and Biorobiotic Systems Group for the help and advice on countless occasions, inspiring discussions and many pleasant hours spent together on- and off-campus.

Table of Contents

List of Figures

List of Tables

List of Listings

1. Introduction

As from 2011, prostate cancer is the second most often diagnosed type of cancer in males worldwide with 903,500 newly diagnosed cases per year and the sixth most often cause of cancer related death with 258,400 deaths per year [18]. A procedure, which has established itself as an efficient and successful treatment option for prostate cancer is prostate brachytherapy. In this procedure, needles are used to place seeds in the prostate in order to eradicate cancerous tissue.

This Chapter gives a general introduction to prostate brachytherapy and the issues the procedure faces in regards to its efficiency and precision. Moreover, reasons for these issues and methods for conquering them are introduced. Finally, the motivation and the accompanying extent of the thesis is stated, and a brief outline is given.

1.1. Prostate Brachytherapy

Brachytherapy, which is derived from the Greek word *brachys* (short distance), refers to a minimally-invasive and outpatient medical procedure. It can generally be used to treat cervical, prostate, breast, and skin cancer [15]. Radioactive seeds (cf. Figure 1.2b) are implanted by insertion of needles into cancerous tissue, in our case located inside the prostate, which leads to its eradication. The goal is to expose the cancerous tissue to radiation from immediate proximity in order to achieve an optimal treatment efficiency by decreasing the necessary range of radiation to only the affected region. At the same time, the risk of radiation exposure to nearby body regions is minimized.

The seeds are approximately the size of a grain of rice with a diameter of roughly one millimetre (see Figure 1.2b) and are made of Titanium and Iodine-125. A needle can contain multiple seeds, which are separated by spacers. This way multiple seeds can be placed along the needle insertion axis with only one needle insertion. The seeds remain in the patient's body permanently. The procedure has emerged as an effective, patient-friendly and cost-effective treatment option.

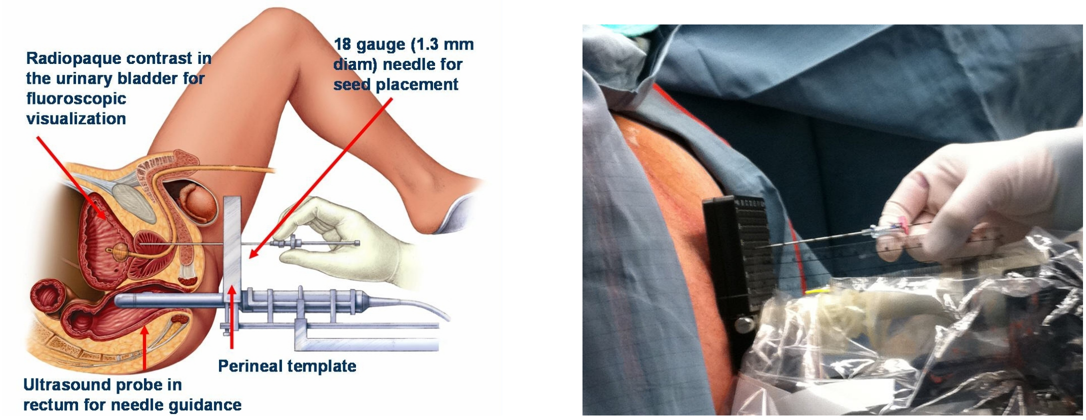

(a) Schematic view of the seed implantation. [2]

(b) View of a prostate brachytherapy procedure as it is currently performed.

Figure 1.1.: The prostate brachytherapy procedure.

In a pre-operative planning stage prior to the brachytherapy surgery, ultrasound (US) images of the prostate are recorded in various, equidistant depths in order to view multiple layers of the prostate. The ultrasound probe is inserted into the rectum, as shown in Figure 1.1a. On the US images specific regions, which determine the boundaries of the prostate, are marked (see Figure 1.2a). These boundaries mark the limits for seed implantation and serve as landmarks in the surgical procedure. A grid layer is placed over the images, which resembles the perineal template (see Figure 1.1a and Figure 1.1b) and will serve as orientation during surgery.

In order to conduct precise needle insertion and to be provided with a stable platform to work on, a so called Brachystepper™ is used. The device, which is shown in Figure 1.3, is mounted to the patient bed and can be adjusted to the necessary location where the procedure is performed. It holds the template and the US probe, which can be advanced and retracted precisely in steps of 5 mm, in order to take US images at these increments.

During the insertion procedure, about 50 to 100 seeds are implanted. The needles containing the seeds are manually advanced, as shown in Figure 1.1b toward the planned locations, where they are then deposited. Ultrasound images taken by the probe visualize the prostate, the needle and the seeds in order to observe whether the seeds are being placed at the correct location (see Figure 1.2a). During insertion, the surgeon has to switch between the layers to obtain an overall view of the needle trajectory, since only two dimensional layers can be recorded. The US image in Figure 1.2a illustrates the marking of the planted seeds. The seed locations are marked by green dots. The green

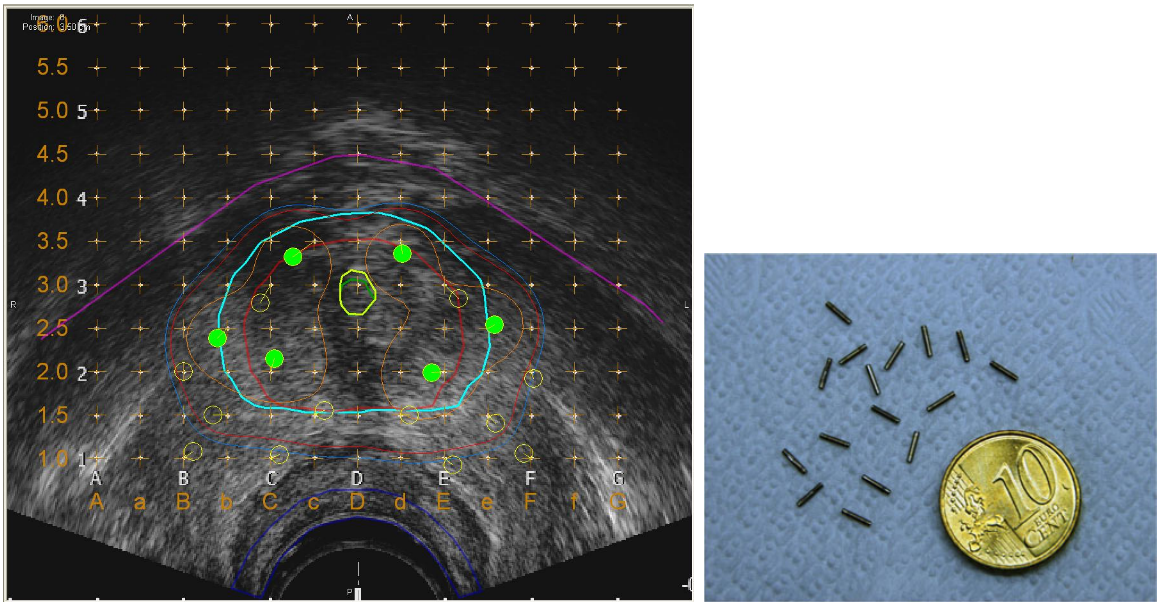

(a) An ultrasound image after a procedure. The green dots resemble the final seed location.

(b) The seeds for implantation. [1]

Figure 1.2.: Ultrasound perspective of the procedure.

circles, which are not filled, represent a spacer at the specific layer. This means that a needle was inserted at this location but did not contain a seed at the observed depth. The green crosses represent the perineal template, thus the initial insertion points of the needle into the skin and furthermore, the ideal location for the seed to be placed. In Figure 1.2a, however, it can be observed that the actual locations of the seeds differ from the ideal position. Some seeds are off by about two to three millimetres. In fact, current manual needle insertion techniques for prostate cancer treatment can place seeds with an accuracy of only five millimetres , which is a substantial error given the average prostate size. As a result, due to delivery of a different radiation dose, the radiation will not have the desired effect on the cancerous tissue and could instead undermine healthy tissue. If the deviation exceeds a certain threshold, corrective measures need to be applied, which is up to now done manually. The deflection of a needle while it is being inserted is dependant on multiple factors, which will be introduced in the following section.

1.2. Influences on the Precision of Seed Placement

The predominant causes of inaccuracy in seed placement are needle deflection and tissue deformation during needle insertion/retraction [21, 25]. This is due to the physical and

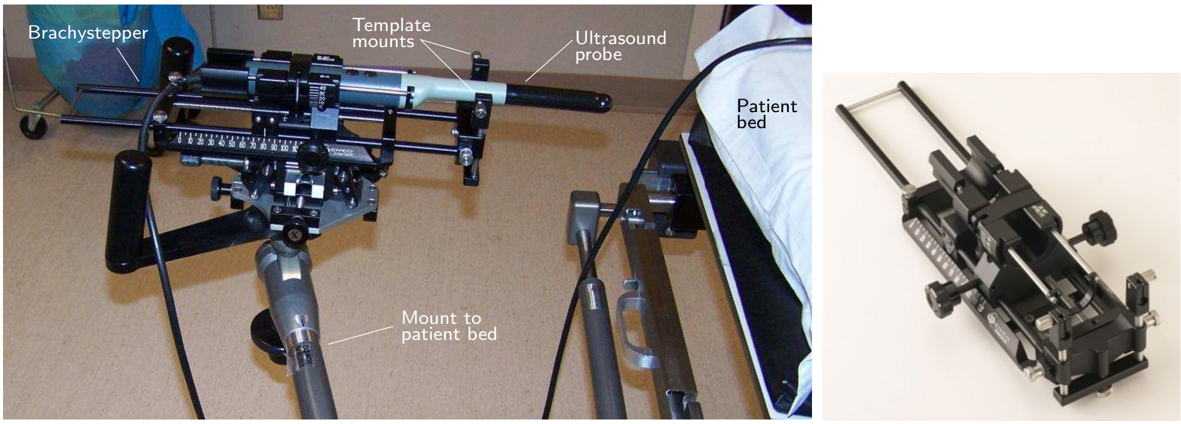

(a) The Brachystepper$^{\text{TM}}$ mounted onto the stand.

(b) The Brachystepper$^{\text{TM}}$

Figure 1.3.: The equipment used for prostate brachytherapy.

geometrical properties of the needle [13, 19] and the tissue structure [26]. One of the major reasons for deflection is the shape of the needle tip. In prostate brachytherapy, the needle tip is bevelled, which means that the tip is asymmetric. As a result, the displacement of tissue at the tip during insertion is also asymmetric [23]. A larger amount is displaced at the side of the bevel. This leads to an increased proportion of force acting in perpendicular direction to the needle axis on the needle tip. The force builds up on the side of the bevel (see Figure 1.4a), which ultimately is responsible for a curved needle trajectory. Webster et al. [26] found in 2005, that the amount of deflection is dependent on the bevel angle. They tested various angles ($5°$ to $80°$) and concluded that needles with smaller bevel angles tend to more bending than needles with steeper bevel angles. This can be attributed to the fact that the forces acting on bevelled tips with smaller angles have a higher component in the perpendicular direction in respect to the needle axis (see vector P, Figure 1.4b). Figure 1.4c depicts how the bevel angle is measured.

Another influencing factor, especially for the amount of needle bending, is the needle diameter. Okamura et al. [23] researched the forces acting on a needle during insertion and found that relatively small needle diameters lead to more needle bending because of their lower resistance force, where as larger needle diameters show a reversed effect.

Generally it can be stated that needle deflection and tissue deformation are coupled effects and influence each other. A result pertinent to the work presented in this thesis is that when a beveled-tip flexible needle is pushed through tissue, the asymmetry of the tip causes the needle to bend. Since this feature leads to a certain degree of predictability, it can be utilized to steer the needle into a desired direction.

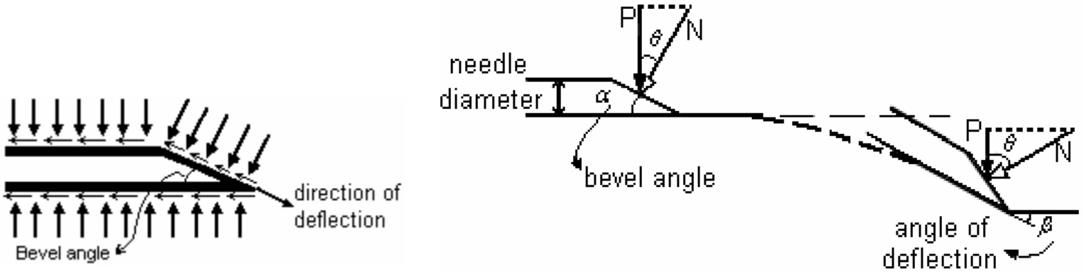

(a) Forces acting on the needle bevel and the needle shaft. [11]

(b) Force components at the needle tip. [11]

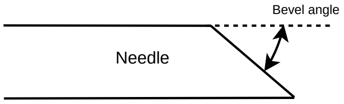

(c) The angle measurement of the needle bevel.

Figure 1.4.: Forces acting on a bevel tip needle during insertion.

1.2.1. Correction of Deflection

A main idea related to needle steering is to leverage the very tendency of the bevel-tip needle for travelling on a curve to bring the needle tip back on the intended path once the needle has been bent, regardless of what caused the needle deflection [8]. To this end, the needle's bevel location can be changed by a feedback control algorithm based on the *real-time feedback of needle deflection*. The feedback control algorithm will steer the needle into the opposite direction when needle deflection exceeds a set threshold by simply turning the needle about its longitudinal axis by 180°. This causes the forces acting at the needle tip to point in the opposite direction and steer the needle back toward the unbent ideal path.

1.3. Motivation

In order to conduct needle steering to correct the trajectory, sensing the deflection is an important prerequisite. Incorporating a *physical sensor* for measuring this quantity directly is next to impossible in a clinical setting, at least with the current technology. To measure the needle deflection during insertion into soft tissue, one may consider using 3D ultrasound imaging. However, detection of the typical needle tip deflections in the order of several millimeters will be difficult due to the low resolution of ultrasound images and the associated high computational demands, notwithstanding the high costs of integrating a 3D imager and the required image processors in a computerized needle insertion system. Using 2D ultrasound imaging is not suitable either because deflection measurement requires that the needle be always visible in the image plane while in practice the surgeon needs to intermittently switch between various sagittal and axial planes to monitor the insertion progress. Another possibility to measure the needle deflection is to use an electromagnetic tracking system, such as the Aurora Electromagnetic Tracking System by NDI, which involves a sensor embedded in the needle. However, this is only appropriate for in-vitro testing where invasiveness is not an issue; sterilization requirements and the pre-loading of seeds inside the needle make in-vivo utilization of a tracker inside the needle prohibitive. Therefore, a non-invasive virtual sensing approach to needle deflection measurement in soft-tissue needle insertion is pursued. The deflection could simply be measured at the needle itself using the measurable forces and torques at the base of the needle. These forces would be related to the forces/moments acting along the needle, which are ultimately responsible for the needle tip deflection.

The resulting estimation of needle tip deflection is a large part of this work's contribution. The real-time measurement of needle deflection using a *virtual sensor*; The foundation of the virtual sensor is the theory that the transverse force and the bending moment at the needle base predict the needle's longitudinal deflection inside the tissue [20, 24]. Therefore, as the needle is being inserted into tissue, the forces and moments reflected at the needle base are measured by a physical sensor. Then, a needle tip deflection model and virtual sensor are developed solely based on this force/moment at the needle base. This virtual needle deflection sensor could be applied not only to prostate brachytherapy procedures but to a wide range of percutaneous medical procedures that involve needles prone to deflection. Its simplicity in terms of the use of hardware components and equipment is perhaps one of the most notable strengths of this approach. The most expensive peace of hardware involved in the system would be a force sensor, which is, compared to other equipment used in surgery, very cost-effective.

The virtual sensor is incorporated into a hand-held robotic assistant system. The system is intended to support the surgeon during prostate brachytherapy. As it requires to be used easily and intuitively, the setup should be kept as simple as possible, which will also keep the overall system cost-effective. The basic idea is illustrated in Figure A.1 of the appendix. Here, the hand-held assistant is guided by a rail, which restricts motions to the direction of the needle axis and thus the direction of insertion. As can be seen, needle insertion with the hand-held assistant is done manually. This means the surgeon is fully in charge of inserting the needle and the computerized system only modifies the bevel location. Consequently, the projected hand-held instrument will be intrinsically safe to use. The sensorized template shown in Figure A.1 was omitted for the sake of simplicity in the first design of the assistant system and later on added to the setup.

A further reaching design proposal of the assistant system, which provides an alternative way of guiding the needle towards the intended trajectory, is illustrated in Figure A.2 of the appendix. A second template behind the sensorized template is used to apply force perpendicular to the needle axis. This leads to the compensation of the needle bending related to tip forces and the needle is guided back to the desired trajectory. As this system is obviously far more advanced than the version shown in Figure A.1, its design exceeds the scope of this thesis, but was nevertheless mentioned in order to provide an initial idea about where this research will be headed in the future.

In summary, the aim of this thesis was to develop a first prototype for a low-cost and effective hand-held instrument for use in prostate needle insertion that automatically corrects the needle tip's bevel location during manual insertion in order to improve needle targeting and seed placement accuracy.

1.4. Outline of the Thesis

The thesis is divided into six chapters, following Chapter 1. Chapter 2 reviews relevant publications for this research. It is succeeded by Chapter 3, which provides a detailed description of the assistant system. Particularly design aspects such as the used mechanical, hardware and software components and their interaction are introduced. Moreover, the reason for using the mentioned components are justified. The virtual sensor for estimating the needle tip deflection mentioned in Chapter 3 is further introduced in Chapter 4. This is done by explaining the mathematical model, which constitutes the force sensor based virtual sensor. Subsequently, the needle model is validated by comparing the estimated to the measured deflection. In order to show the advancement in terms of precision of this model over a similar, prior to this thesis proposed deflection model, both model estimations are compared. In the next step, a sensorized template is used together with the assistant. Chapter 5 elaborates the measuring of forces/moments at the template and the particular setup. The issues involved with the measurement of forces and moments based on experimental data will be identified and suggestions for necessary future improvements made.

Chapter 6 discusses strengths and weaknesses, as well as necessary changes and improvements to the assistant prototype, virtual sensor and sensorized template. Furthermore, the remaining work for the immediate future for all three previously mentioned aspects, is proposed. Finally, Chapter 7 provides a brief summary by giving the conclusion of the work, which was presented in this thesis.

1.5. Publication

Parts of this thesis will be published in the form of a research article in the special issue *Sensors for Robotics* of the *Journal of Sensors* by the Hindawi Publishing Corporation [22]. Among the published contents are parts of Chapter 1, Chapter 3 and parts of Section 4.1, Section 4.2, Section 4.3 and Section 4.4 of Chapter 4. Portions of the discussion in Chapter 6 and conclusion in Chapter 7 will also be published in the same article.

2. Literature Review

Needle deflection in soft tissue has been researched for over a decade and several contributions have been made in the field. Several studies have been published, which attempted to model the relations between forces and moments at the needle base to needle deflection in soft tissue. The most relevant literature for this thesis will be reviewed in this chapter. Some models, which will be reviewed, are based on the Euler-Bernoulli beam theory. The theory provides a means of calculating the deflection of cantilever beams under load.

Kataoka et al. [19] in 2001 proposed a first model, which uses a distributed load along the inserted section of the needle to estimate the deflection at the needle tip. Their model relates the force on the needle base to the needle deflection while it is inserted into tissue. They introduced the infinitesimal force per length (ω), which was predicted to be constant over the insertion length of the needle. ω can be also seen as a distributed load along the inserted part of the needle. They described the shear force (F_{end}) at the needle base by

$$F_{end} = \int_0^{l_{in}} \omega(l,d) l \, dl \tag{2.1}$$

where l_{in} is the insertion depth, l is the axial position of the needle with the origin at the needle tip and $\omega(l,d)$ is the infinitesimal force per length on the needle side. In order to calculate the needle deflection, the following model was proposed by Kataoka et al.:

$$\begin{aligned} g(l,d) = \frac{W(d)}{24EI}(l^4 - 4l_{in}(l_{in}^2 + 3l_{in}l_{out} + 3l_{out}^2)l \\ + l_{in}(3l_{in}^3 + 12l_{in}^2 l_{out} + 18l_{in}l_{out}^2 + 8l_{out}^3)); \; (0 \leq l \leq l_{in}) \end{aligned} \tag{2.2}$$

where $g(l,d)$ is the needle deflection, l_{in} is the length of the needle inside the tissue and l_{out} is the length of the needle outside of tissue. Since F_{end} increases statically while the needle is being inserted into the tissue with constant velocity, Kataoka et al. made the assumption that $\omega(l,d)$ stays constant ($W(d)$) throughout the insertion. To evaluate the model, a needle was inserted into swine's hip muscle. During insertion,

F_{end} was measured continuously and X-ray images were recorded continuously in order to measure the needle deflection. Their results however showed an offset in the estimated tip deflection. They concluded that their model underestimates the deflection outside of tissue, which leads to the offset.

Abolhassani et al. [9–11] proposed a different model, which also relates the forces along the needle to the base forces and moments. Their model is also based on the Euler-Bernoulli beam theory but with different force assumptions along the needle. Their model was based on the assumption that the sum of all forces along the needle is comprised of the vertical component of the cutting force at the bevelled needle tip, a triangularly distributed resistance force and the shear force and bending moment at the needle base. The triangularly distributed load, however, was not considered relevant in the model as its impact was negligible. The proposed model for needle tip deflection (ν) was

$$\nu = \sum_{i=0}^{n} (3\Delta M_{r_i} L^2 - \Delta F_{r_i} L^3)/6EI \tag{2.3}$$

where n is the amount of necessary steps for a certain depth inside tissue and ΔM_{r_i} and ΔF_{r_i} are the changes of the force and moment at the needle base in between two insertion steps.

Since the shape of the bevelled tip will not change during insertion, the perpendicular portion of the cutting force at the needle tip stays constant as well. As the perpendicular forces (shear forces) at the needle base are steadily increasing during insertion, as will be shown in Chapter 4, the above made assumption of only including the cutting force in the deflection model, is not valid. Both models introduced by Kataoka et al. and Abolhassani et al. solve the Euler-Bernoulli equation in the static domain.

Other studies have tried to decouple the coupled effects of tissue deformation and needle deflection by considering one of two extreme cases: a rigid needle in deformable tissue or a flexible needle in rigid tissue. For the second case, a bicycle-like kinematic model predicting the needle tip position was proposed by Webster et al [27].

An analytical model also based on the Euler-Bernoulli equations but in the dynamic domain was proposed by Asadian et al [14]. They used Green's functions to determine the closed-form solution of the partial differential equations for needle deflection. To model the tissue elasticity, discrete virtual springs were used along the inserted portion of the needle.

Abolhassani et al. in 2004 [12] investigated the effects of several methods of needle rotation. They tested several methods for rotating the needle about its axis, which were no rotation, continuous rotation, partial rotation with different angles and rotation with force control. It was found that rotational motion in general reduces friction and tissue displacement and that needle rotation should be utilized in needle insertion procedures. It was furthermore concluded that to control the needle rotation such that the forces remain at a minimum is the best approach.

3. The Surgeon’s Assistant Prototype

In this chapter, the setup of the assistant prototype is introduced. Information about the requirements to conduct needle insertion experiments is provided. Furthermore, the chosen mechanical components, hardware and software of the robotic system prototype with two degrees of freedom (DOF) are introduced.

3.1. Requirements

As an assisting system, the control of insertion should at all times during needle insertion remain in the hands of the surgeon, as this grants the safe use of the system. To increase the precision of insertion, the needle motions should be restricted to the translational motion required for insertion. Hence, the insertion motion the surgeon performs should be guided by e.g. a rail-carriage system, which represents a one-DOF linear stage. This linear stage only allows translational motions in the direction of needle insertion. The rail-carriage system should be virtually frictionless but at the same time provide high precision.

One additionally necessary degree of freedom is rotation of the needle about its longitudinal axis. This rotation should be automated and controlled by software algorithms. The automated rotation of the needle will not have the potential to reduce the safety of the procedure significantly, as the amount of kinetic energy induced by needle rotation is very low. Also, by measuring the torque during needle rotation, the energy induced by needle rotation can be directly measured and limited if necessary.

For the prototype introduced in this chapter, besides manual insertion, also automated insertion is desired, in order to have the ability to conduct a wider range of experiments, in which fully automated insertion can be tested. This means the possibility should be provided to connect the carriage for translational motion to a motor. The motor should,however, be entirely detachable from the carriage, so that motor inertia will not affect manual insertions.

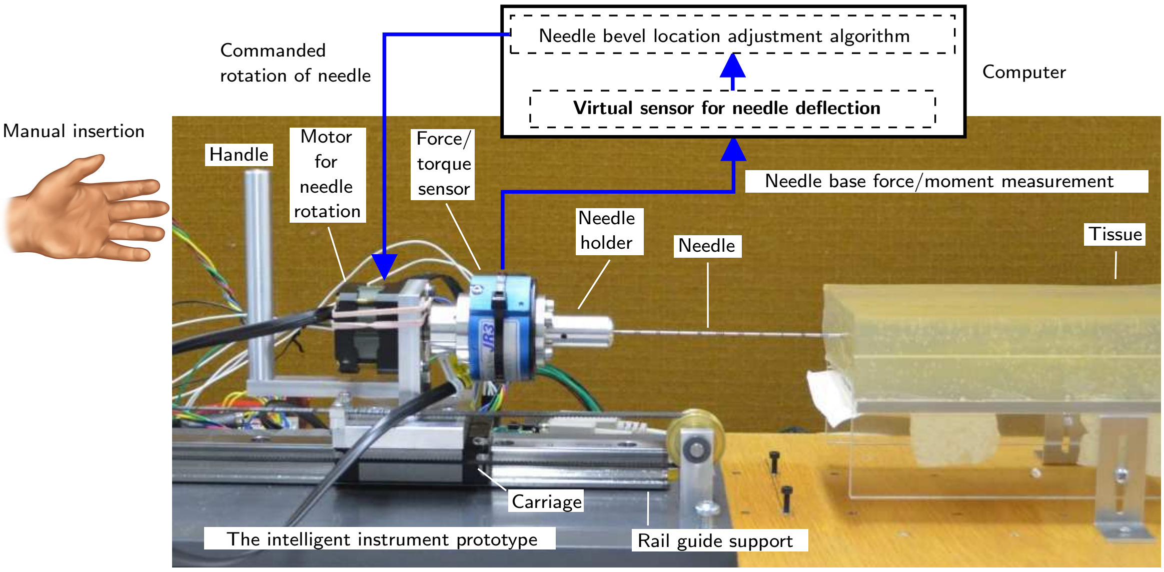

(a) Labelled side view of the system.

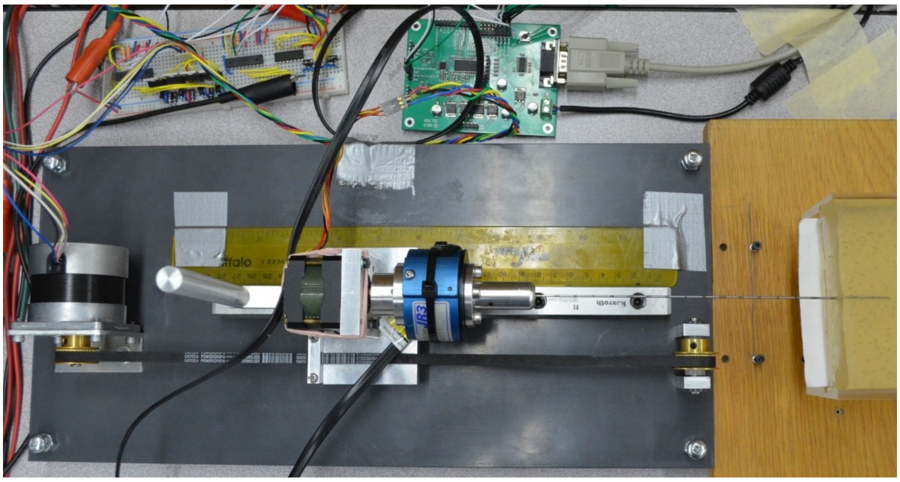

(b) Top view of the system.

Figure 3.1.: The setup of the surgeon's assistant prototype.

One further requirement is a high modularity of the system. As a common issue for a prototype, certain components might not work as desired and need to be exchanged. This calls for a system, which consists of modules that are relatively independent from each other and can therefore be interchanged easily. It also means that most of the assembly should be custom made.

Figure 3.1 shows a labelled side view (Figure 3.1a) and a top view (Figure 3.1b) of the assistant system prototype. It also illustrates the incorporation of the force sensor based virtual sensor and the feedback loop for needle trajectory correction.

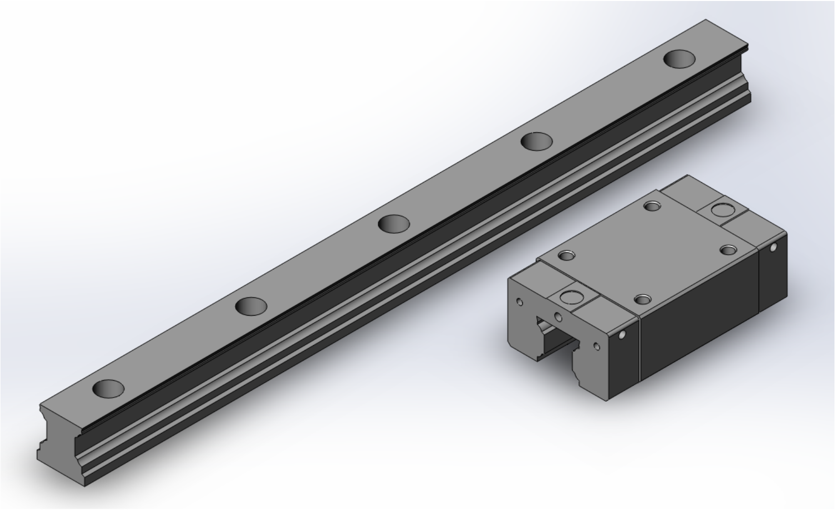

Figure 3.2.: A CAD model of the pre-built rail and carriage. The CAD models of rail and carriage were obtained from mcmaster.com [3].

3.2. Mechanical Components

For the linear stage, a ball-bearing mounted rail-carriage system made by Rexroth was chosen. These systems are especially designed to provide high rigidity and precision. They are also used in machine tools and industrial robots [6]. Figure 3.2 shows a CAD model of the rail and carriage. The rail system can absorb loads of equal magnitudes in the two horizontal and two vertical directions, meaning that the rail could be mounted horizontally or vertically while being able to carry weights of the same magnitudes in both positions. This would also enable a certain independence in regards to vertical or horizontal mounting of the system. Since also the friction forces of the linear stage should be virtually non-existent, this pre-built rail-carriage system was chosen. With these types of systems, the carriage and rail are specifically matched and designed for each other such that friction can be assumed to be a negligible factor.

Although fully motorized linear stages can be obtained, this alternative was not considered. Using a system with custom attachments for a motor increases the modularity of the assembly and makes custom designs for motor coupling and decoupling possible. This is important because, as mentioned, inserting the needle into tissue will not only be done in an automated fashion with a motor, but also manually. To connect the carriage to a motor, a timing belt is used, which is simply clamped to the carriage when necessary. When the carriage is disconnected from the timing belt, the carriage can be moved freely with only the rail-carriage friction affecting translational motions. Using a timing belt and timing pulley on the carriage motor is important, because the belt

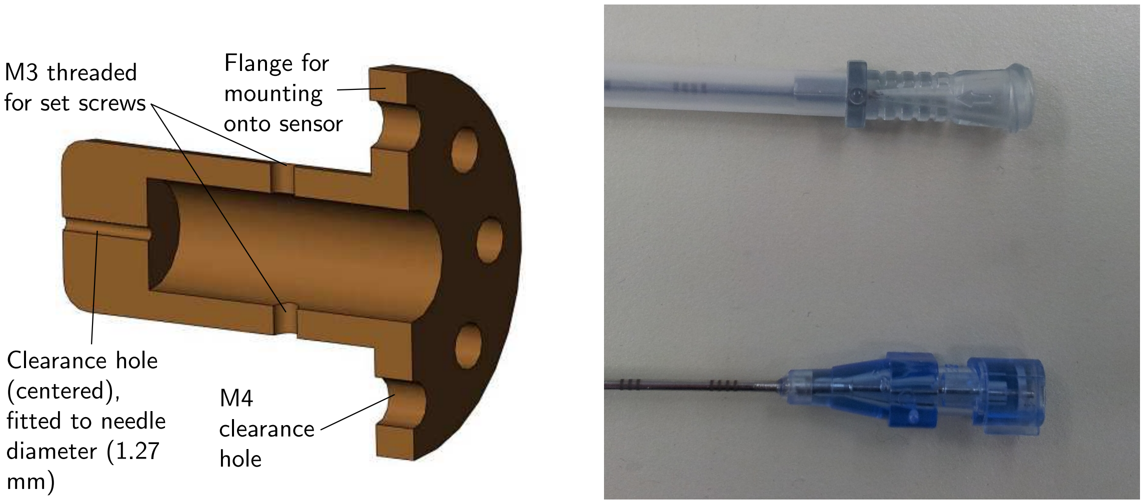

(a) A CAD model of the needle holder. The model was cut through the middle of the holder to show the interior.

(b) The handles of the used brachytherapy needles.

Figure 3.3.: The needle holder and handles of the used brachytherapy needles.

should not slip, as the rotary position of the carriage motor shaft is used for position control of the carriage. Details about the used motors are further explained in Section 3.3.1. The carriage motor mount, which fixates the motor to the ground plate, can be shifted back and fourth in the same direction as the timing belt. This can be used to adjust the tension of the belt. Slots were milled into the motor mount in order to enable motor position adjustment. Illustrations of the assistant system's CAD model from three different perspectives are given in Figure A.3, Figure A.4 and Figure A.5 of the appendix.

On the carriage, a plate is mounted vertically, which holds the motor for needle rotation. The force sensor and needle holder, which is tied to the force sensor, are mounted to the needle motor shaft. This way, the force sensor and needle motor shaft are in line with the needle axis. The needle holder, which is shown in Figure 3.3a, fixates the hand piece of the needle (see Figure 3.3b) via two opposing set screws. Also attached to the carriage is a handle to perform manual insertions.

The entire assembly is mounted onto a ground plate, which is made of PVC (see Figure A.3 of the appendix). Each component, such as carriage motor and rail are mounted on to the ground plate individually, with only the belt connecting the rail-carriage system and carriage motor. This way, the position of rail and motor on the ground plate can be adjusted individually, which can be important in case the motor in use needs to be replaced with a motor of different measures. The ground plate also has four screws mounted vertically on each edge (see Figure 3.1b; not present in the CAD model in Figure A.3) to adjust the height and level of the whole assembly. To increase the grip, rubber bumpers were fixed onto each screw.

3.3. Hardware

The hardware of the setup involves two stepper motors and a force sensor. Both motors are interfaced to a PC by a HILINK data acquisition (DAQ) card. The JR3 force sensor is interfaced via a PCI card. Specifics about the used hardware will be introduced in the following sections.

3.3.1. Motors

The chosen motors are stepper motors. For slow rotational velocities, which are predominantly the case for needle insertion experiments, stepper motors generally provide high torque. With increasing rotational velocity, however, the torque decreases rapidly. Since in our case the maximum velocity of the carriage will not exceed 15 mm/s, as this is the highest insertion velocity for needle insertions, a lack of torque is not an issue. The motor to drive the carriage is a *TEC SPH 54AB 116* unipolar stepping motor, with a minimum resolution of 1.8° per step. The needle motor is of type *LN.S4529*, manufactured by *Sankyo Seiki Mfg Co. Ltd.* and has the same step resolution as the carriage motor. More technical details about the stepper motors are provided in Section B.1 of the appendix.

Since the time for this project was rather limited, the duration for implementing the system's hardware and software was a critical aspect. This leads to a further tendency towards using stepper motors. A predominant advantage of stepper motors over DC motors is their ease of control. The position can be controlled without the necessity of a feedback loop, since stepper motors are frequency controlled. One upward edge assigned to the motor controller means one discrete rotational position change of the motor shaft. The position is controlled by the amount of steps given to the controller and the speed can be controlled by the frequency of these steps. With the mentioned resolution of 1.8° per step, 200 pulses are necessary for a full revolution of the shaft. If the pulses are provided with a frequency of 200Hz, the motor's rotational speed is one revolution per second.

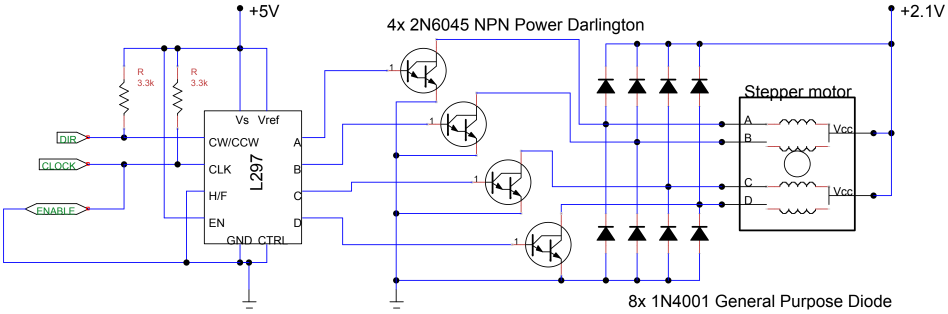

(a) The driver circuit used for the carriage motor.

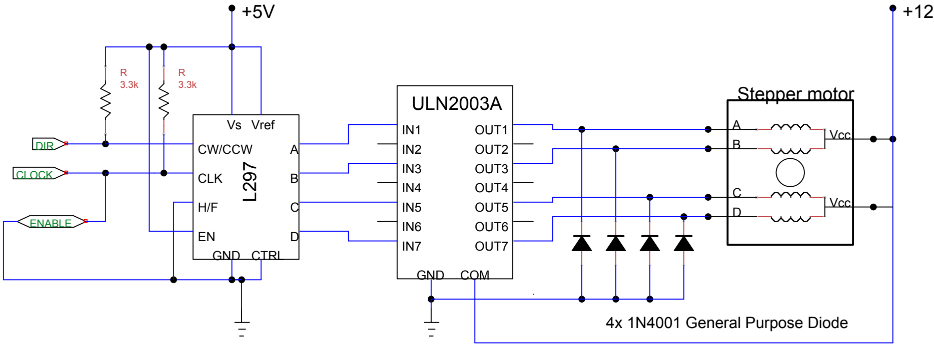

(b) The driver circuit used for the needle motor.

Figure 3.4.: The driver circuits used for the unipolar stepper motors. [4]

Another reason for favoring stepper motors was the availability of the motors. Being salvaged parts from printers or similar hardware, there were no additional expenses. The downside of this, however, was that there were no data sheets available for the motors. Hence, the correct wiring had to be obtained by resistance measurements between wire pairs. Specifics about the measurements are given in Section B.1 of the appendix.

The disadvantages that come with the stepper motors are limited resolution and the distinctive choppy motions, especially when the rotational velocity is slow. The vibrations resulting from this can influence force and torque measurements. On the other hand, small vibrations in the needle could decrease the amount of friction between tissue and needle. To drive the motors, a control circuit is necessary. The design of these circuits will be explained in the following section.

3.3.2. Motor Control Circuit

The control circuit for the stepper motors, which is shown in Figure 3.4, consists of a L297 stepper motor controller IC and a power stage. The controller provides the logic for the power stage, which is comprised of Darlington transistors. Darlington transistors were chosen due to their availability. For future designs, MOSFET drivers could be used, since their R_{DSon} (resistance between drain and source) is low, which means the current for a connected motor increases. Also, the lack of a gate-source current could decrease the load on the controller. For the needle motor, a ULN2003A Darlington transistor array, which provides up to $500mA$ is sufficient, as not much power is required to turn the needle. For the carriage motor, four high power Darlington transistors were used, which allow a higher current flow. The current drawn by the carriage motor is roughly $1A$.

Interfacing a PC

The inputs *clock*, *direction* and *enable* for the control circuits are provided by a *HILINK* real-time hardware-in-the-loop control platform. Two frequency outputs provide the clock signal and digital outputs provide the direction and enable signals. The enable signal, however, is not connected to the enable input of the controller. If the signal is set to "low", it connects the clock signal to ground (see Figure 3.4). This way, turning the motor is disabled but the motor is still locked and not free spinning as opposed to if the enable signal were connected to the controller enable input. Theoretically the motor should also stop and be locked when the clock is set to zero. Since, however, the frequency outputs of the HILINK board never output zero but always remain on a frequency of approximately 0.5Hz, this precaution is necessary.

There are two ways for operating the HILINK board in real-time; hard real-time and soft real-time operation. If hard real-time operation is used, the Simulink model controlling the board must be set to "external mode". The model then runs on MATLAB's Real-Time Windows (RTW) kernel, which is completely separated from the kernel of the PC's operating system (OS). When using soft real-time operation, the model controlling the board can be run in "normal mode". In "normal mode" the models run on the kernel of the PC's OS. The variety of Simulink blocks provided by the Simulink library, which can be used in soft real-time operation is much higher, although the sampling rate is very limited. With the developed models used for conducting insertion experiments, the sampling rate is limited to approximately 20Hz. The reason is that the models are running on the non-real-time OS kernel, which has a variety of tasks to focus on at the same time and not only focuses the CUP's processing power on the Simulink model execution. If therefore the sampling rate is set too high, the sample time is too low for

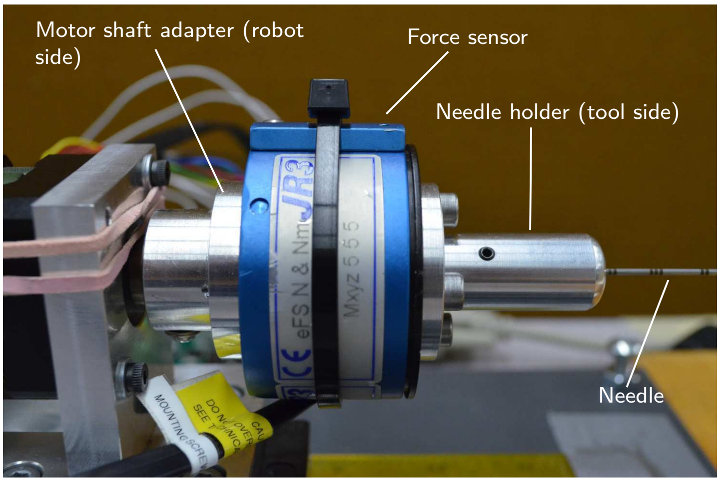

Figure 3.5.: A close-up view of the force sensor as mounted onto the setup.

the model to execute in time in every sample interval. This means that the model will cease to run in real-time. The RTW kernel on the other hand ensures that the executed model runs in real-time unless a sampling rate limit is reached, which is in the range of several thousand Hertz. If this limit is reached, the RTW model will not execute at all. In this setup it was only possible to use the soft real-time approach. The reason is explained in Section 3.4.

The platform is connected to a PC via a serial communication (RS232) and interfaced in MATLAB/Simulink. Further information about the specification of the HILINK board can be found in chapter B.2 of the appendix.

3.3.3. Force Sensing

To sense forces at the needle base, a 6 DOF JR3 force sensor of type 50M31A-I25 is used. The sensor is mounted onto the needle motor shaft, as shown in Figure 3.5. The z-axis of the sensor points to the same direction as the longitudinal needle axis. The attached needle holder was specifically made such that the direction of the bevelled tip points to the same direction as the y-axis of the sensor. A rotation of the sensor frame about the z-axis to adjust the frame to the the bevel direction is therefore not necessary.

The sensor's captive bolts allow for directly tying the sensor to the motor shaft adapter. The face plate of the motor shaft adapter is mirrored at the tool side of the sensor (see Figure 3.5), so that the needle holder and motor shaft adapter can be directly attached to each other. This is important for the case that insertion experiments need to be conducted without using a sensor at the needle base. The needle holder can be directly connected to the motor shaft adapter when the force sensor is detached.

The relevant moments for deflection measurement occur at the tip of the needle holder (see Figure 3.5). Since the sensor measures moments about its centre, recorded moments need to be recalculated in order to acquire the relevant moments for deflection. The moment (M_H) acting at the tip of the needle holder can be expressed as

$$M_H = M_S - F_S\, l \tag{3.1}$$

where M_S and F_S are the moment and force measured by the sensor and l represents the distance from the centre of the force sensor to the tip of the needle holder (52.75 mm). Further information about and technical details of the force sensor are provided in section B.3 of the appendix.

3.4. Software

The software for the setup runs on a 32 bit PC, on which the Microsoft® Windows™ XP operating system is installed. For ease of control and to avoid the programming burden a language such as C/C++ would imply, it was desired to program the assistant prototype in MATLAB/Simulink. Simulink also comes with a large variety of tools to facilitate the work with prototypes such as this one. Because the HILINK board is also interfaced in Simulink, using Simulink suggests itself.

Communication with the force sensor is established via a C application programming interface (API). In order to read data from the sensor in Simulink, a C S-Function needed to be written. Generally, an S-Function provides a way of running C/C++ code in Simulink models. The S-Function comes with a specific structure of C-functions, with which C-code used in the S-Function, such as the force sensor code, must comply. Before execution in a model, the code is compiled in MATLAB into a MEX file, which is then integrated into the S-Function block. This block can finally be used in Simulink models.

In the sensor's S-Function, the three functions *mdlStart()*, *mdlOutputs()* and *mdlTerminate()* contain the code to communicate with the sensor and to retrieve the force/-torque data. The function *mdlStart()* contains code, which initializes the sensor at the start of each model execution, *mdlOutputs()* reads the force/torque data in every sampling interval and *mdlTerminate()* terminates communication with the force sensor after the model execution has ended. The C code of these functions is provided in Listing C.1 and Listing C.2 of the appendix.

The sensor's API makes use of the OS's Win32 API. Furthermore, the drivers for the sensor's PCI board are made for the Windows OS. Therefore, the Simulink sensor blocks can not be run on the (RTW) kernel, as it does not have access to the Windows OS kernel and thus has no access to the Win32 API and PCI drivers. Therefore, the only option to controlling the system and simultaneously recording forces in real-time is soft real-time operation. This restricts the control to the aforementioned 20Hz, which is a very low sampling rate but enough for our experiments.

To be able to build models for experiments quickly, general functions blocks for controlling the assistant prototype are necessary. These blocks include functions like controlling the motors or reading force data. For this purpose, a small toolkit library was designed. The library contains blocks for moving the carriage, needle turning, force sensor reading and utility methods such as moving average or offset correction. The essential input parameters for carriage control are speed and and travel distance, where the sign of the distance parameter determines the direction of travel. For needle rotation, the essential inputs are angular speed and turning angle, where also the sign of the assigned turning angle determines the direction of rotation. The toolkit library is shown in Figure C.2 of the appendix.

The two predominantly used Simulink models for insertion experiments are illustrated in Section C.2 of the appendix. Figure C.1 shows the model for simple insertion experiments without rotation. Figure C.3 depicts a more complex model for insertion experiments including on-line tip deflection estimation and needle rotation for correcting the needle deflection. Both models use some of the blocks from the toolkit library (see Figure C.2). The experiments for which the just mentioned models were developed are further explained in the following chapter.

4. The Virtual Deflection Sensor

As mentioned in Section 1.3, the virtual sensor is intended to provide a cost-effective and efficient means of detecting the needle tip deflection. For the virtual part, a mathematical model describing the needle tip deflection during insertion is needed. In this chapter, the needle deflection model, which is used to calculate the needle tip deflection from the force/torque data provided by the physical sensor, is introduced. Subsequently, the experimental setup for needle insertion into soft tissue is explained. The results of the experiments conducted with the previously introduced assistant system are then used to verify and show the deflection model's degree of precision by comparing the estimated to the measured tip deflection.

4.1. The Deflection Model

The developed needle model is fundamentally based on a static model for deflection of a cantilever beam. The model was specifically kept in the static domain of the Euler-Bernoulli theory. There is not much and particularly no rapid motion involved during needle insertion, which would suggest the use of a dynamic model. Furthermore, static models can often be kept more simple in terms of involved calculations, and therefore demand less computational power.

The needle can be regarded as a cantilever beam, since its only fixation is at the base. The equations, which are as mentioned based on the Euler-Bernoulli beam theory, relate the loads or forces applied to the beam to its deflection. As the needle deflects increasingly during insertion in soft tissue, it acts as a loaded spring that tries to return to its initial unbent state but is kept in place by the tissue. The needle exerts a distributed load perpendicular to the needle axis onto the tissue. To keep the needle in its bent state, i.e. to maintain the equilibrium condition, the tissue in return reacts with a distributed load along the needle (Figure 4.1). In general, distributed loads can be replaced by a resultant point force (concentrated load) that acts at a specific point along the needle.

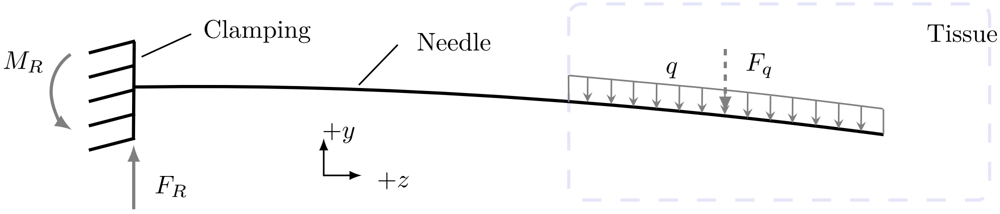

Figure 4.1.: The distributed load q acting along the inserted portion ofe the needle as a reaction force to the needle, as proposed by Kataoka et al. [19]. F_R is the resulting force at the needle base. The 2-D diagram plane is the deflection plane of the needle. The dashed arrow represents the resulting force acting at the geometric centre of the area of the distributed load q.

This reduction allows for a simplification of the equations used to calculate the deflection. The location of the resultant force is the *geometric center* of the area of the distributed load [17]. The magnitude of the force acting on the needle base (F_R) is the integral of the load and can be expressed as

$$F_R = F_q = \int\limits_{L-l_0}^{L} q(z)\ dz \tag{4.1}$$

or

$$F_R = F_q = q \cdot l \tag{4.2}$$

for an equally distributed load, where q is the load per unit length, l_0 represents length portion outside of tissue and l is the length portion of the needle, which is inserted into tissue.

It should be noted that the indicated force at the needle clamping is the resistance force exerted by the clamp onto the needle. While the measured force (F_S) is equal in magnitude to F_R, the directions are opposed. The relation between F_R and F_S can be expressed as

$$F_R = -F_S. \tag{4.3}$$

Since the only support of the needle is at its base, the full magnitude of the resulting force and moment as well as the direction are reflected at the needle base and can be measured. This means that the expected force measurement results should have the same direction as the deflection. Insertion experiments however showed a force at the needle base in opposite direction. Figure 4.7a shows forces and torques for a deflection in negative y-direction. This means that the forces exerted by the tissue can not only

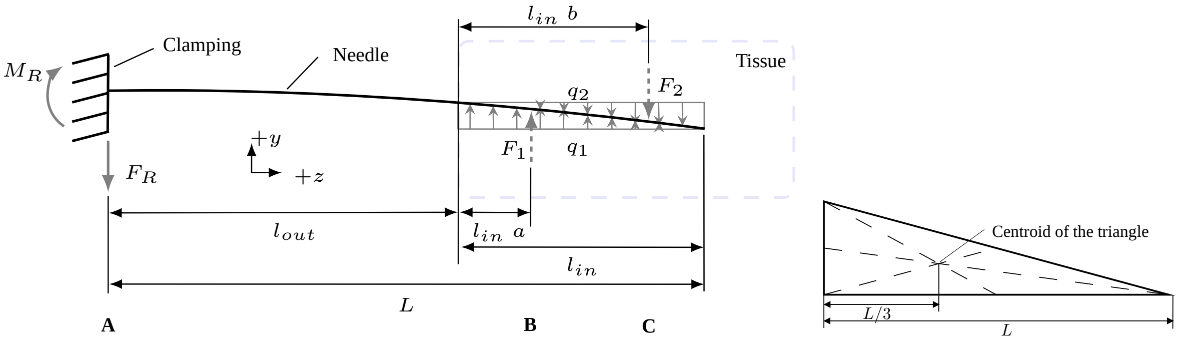

(a) (b)

Figure 4.2.: (a) The triangularly distributed loads q_1 and q_2 acting along the needle while inserting into tissue. F_R is the resulting force at the needle base. F_1 and F_2 - shown with dashed lines - are the resulting forces from the distributed loads q_1 and q_2. (b) The location of the centroid of a triangle.

be one distributed load acting in negative y-direction (cf. Figure 4.1) but must be comprised of multiple loads acting in positive and negative y-direction. Tissue below the needle can be considered as acting as a support and tissue above the needle still exerts a distributed reaction force on the needle.

The triangular distribution of q_1 in figure 4.2a can be explained by assuming that tissue is pushed down more towards the side where the needle enters the tissue. As the needle penetrates deeper into tissue, the deflection increases, which leads to pressure being applied on the tissue in negative y-direction. Tissue, which is horizontally closer to the point of insertion (here: left side, see Figure 4.2a), is exposed to this pressure for an increased period. Therefore the distribution of the load applied on the needle by tissue is at its maximum at the insertion point and decreases in z-direction. This assumption was also made by Abolhassani et al. [10]. They however did not include it in their model, as it had very little impact in their case. For the load above the needle, a reverse effect applies. As the tissue closer to the needle entry point is pushed towards the direction of deflection increasingly, the tissue above the needle in this area can not apply any resistance force from above.

As before mentioned, the loads q_1 and q_2 can be reduced to the concentrated loads F_1 and F_2, which act at the centroid of the triangularly distributed load. The centroid of a triangle and its location is illustrated in Figure 4.2b. The figure shows that the centroid of a triangularly distributed load is at $L/3$, where L is the length of the triangle's leg. Thus, the factors a and b should have the values 1/3 and 2/3 respectively (see Figure 4.2a). It should be noted that the triangular distribution of loads q_1 and q_2 is an assumption.

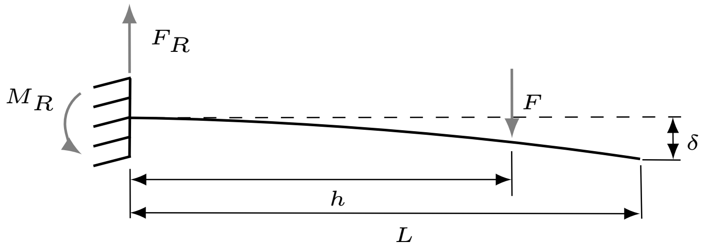

Figure 4.3.: A force and moment diagram for the bending of a cantilever beam with a force F acting at a distance h from the fixation.

A common method to finding deflections in beam structures is twice integrating the bending moment equation

$$M = EI\frac{d^2v}{dt^2} \tag{4.4}$$

where M and v are the moment and deflection at at a distance z from the base, E and I are the Young's modulus of stainless steel (200 GPa) and the area moment of inertia of the needle. The equation for the moment M can be found by analysis of the entire system's free body diagram. The diagram in Figure 4.3 illustrates the effect of a force F, which acts at a horizontal distance h from the beam fixation. The reactive force F_R and moment M_R to F are exerted by the fixation. The bending of the tip δ can be calculated with

$$\delta = \frac{F\,h^2(3L-h)}{6EI} \tag{4.5}$$

([16, p. 1084]) where F is the concentrated load applied on the beam, h represents the distance of F from the beam fixation and L is the overall length of the beam. Equation (4.5) is a result of integrating (4.4) twice for the case illustrated in Figure 4.3. It serves as basis for the developed deflection model.

The difference from the above shown general case of beam deflection to our specific case is that there are multiple forces acting simultaneously (F_1 and F_2) at different locations. Therefore, the method of superposition needs to be applied. This method allows for regarding multiple forces acting separately on the beam and superimposing the deflections resulting from each force [16]. The deflections for each force are

$$\delta_1 = \frac{F_1\,(l_{out}+l_{in}\,a)^2\,(3L-l_{out}-l_{in}\,a)}{6EI} \tag{4.6}$$

$$\delta_2 = -\,\frac{F_2\,(l_{out}+l_{in}\,b)^2\,(3L-l_{out}-l_{in}\,b)}{6EI} \tag{4.7}$$

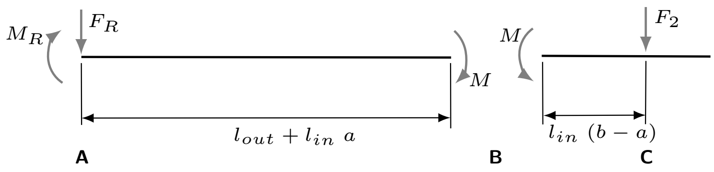

(a) The free body diagram of the bending moments acting at a cut at point **B**. F_R and M_R are the resistance force and moment of the clamping and are both measured by the attached sensor.

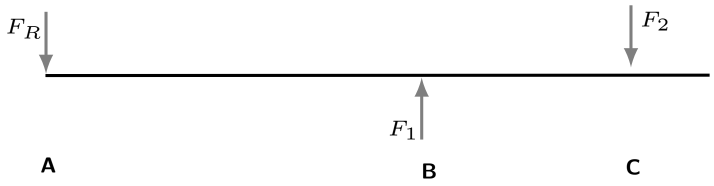

(b) The free body diagram of the forces acting perpendicularly along the needle.

Figure 4.4.: Free body diagrams of the needle while inserting into tissue.

where δ_1 and δ_2 are the deflections at the needle tip for F_1 and F_2 respectively, l_{in} and l_{out} are the length proportions inside and outside of tissue, L represents the total needle length and a and b are factors to adjust the points at which force F_1 and F_2 act. Superimposing the two deflections results in

$$\begin{aligned}\delta_{1,2} =& \frac{F_1\ (l_{out} + l_{in}\ a)^2\ (3L - l_{out} - l_{in}\ a)}{6EI} \\ &- \frac{F_2\ (l_{out} + l_{in}\ b)^2\ (3L - l_{out} - l_{in}\ b)}{6EI}\end{aligned} \tag{4.8}$$

where $\delta_{1,2}$ is the deflection at the needle tip for forces F_1 and F_2 combined. The up to now unknown forces F_1 and F_2, with which a relation to F_R and M_R can be established, can be obtained from the equilibrium conditions. These equilibrium conditions apply in the force and moment system of the free body diagrams in Figure 4.4. The cut in the free body diagram was chosen because in this case, the force F_1 will cancel out at both sides, as F_1 acts in the same direction at both sides of the cut. Force F_1 at point **B** can also be regarded as as support, which means that no shear forces are acting at the cut. Since in every point during the insertion equilibrium conditions are assumed, the moments acting at both the left and right side of **B** must sum up to zero.

$$\begin{aligned}
\text{Left side: } \sum M &= -M_R - M + F_R(l_{out} + l_{in}\ a) = 0 \\
\Leftrightarrow\ M &= -M_R + F_R(l_{out} + l_{in}\ a) \qquad (4.9) \\
\text{Right side: } \sum M &= M - F_2\ l_{in}(b-a) = 0 \\
\Leftrightarrow\ M &= F_2\ l_{in}(b-a) \qquad (4.10)
\end{aligned}$$

As the bending moments at each side of the cut must be equal, (4.9) and (4.10) can be equalized to

$$\begin{aligned}
&- M_R + F_R\ (l_{out} + l_{in} a) = F_2\ l_{in}(b-a) \\
&\Leftrightarrow F_2 = \frac{-M_R + F_R\ (l_{out} + l_{in}\ a)}{l_{in}(b-a)} \qquad (4.11)
\end{aligned}$$

and F_2 can be obtained. The force F_1 can be obtained from the free body diagram in Figure 4.4b. The sum of the forces acting perpendicularly along the needle must also be zero.

$$\begin{aligned}
&\sum F = F_1 - F_R - F_2 = 0 \\
&\Leftrightarrow F_1 = F_R + F_2 \qquad (4.12)
\end{aligned}$$

Although here, only deflection in the 2D-plane is regarded, the model can be easily transferred to 3D, provided a 4 DOF force/torque sensor is used. Also the deflections can be measured in both directions. If the needle deflects into positive y-direction, all forces and moments, including forces/torques measured at the needle base, will simply point into the opposite direction.

4.2. Experimental Setup

To conduct insertion experiments into phantom tissue, the robotic system as it is explained in Chapter 3 was used. Figure 4.5a shows the experimental setup with a camera used for recording the needle path inside tissue. Figure 4.5b shows the top view with the needle deflecting inside tissue. The used phantom tissue for the insertion experiments is liquid plastic, which is made of plastisol and produced by M-F Manufacturing Co. The stiffness of the plastic can be adjusted by the amount of added plastic softener. The thickness of the homogeneous tissue is roughly four centimetres, which provides enough weight to prevent too much shifting along the insertion axis during insertion. If the

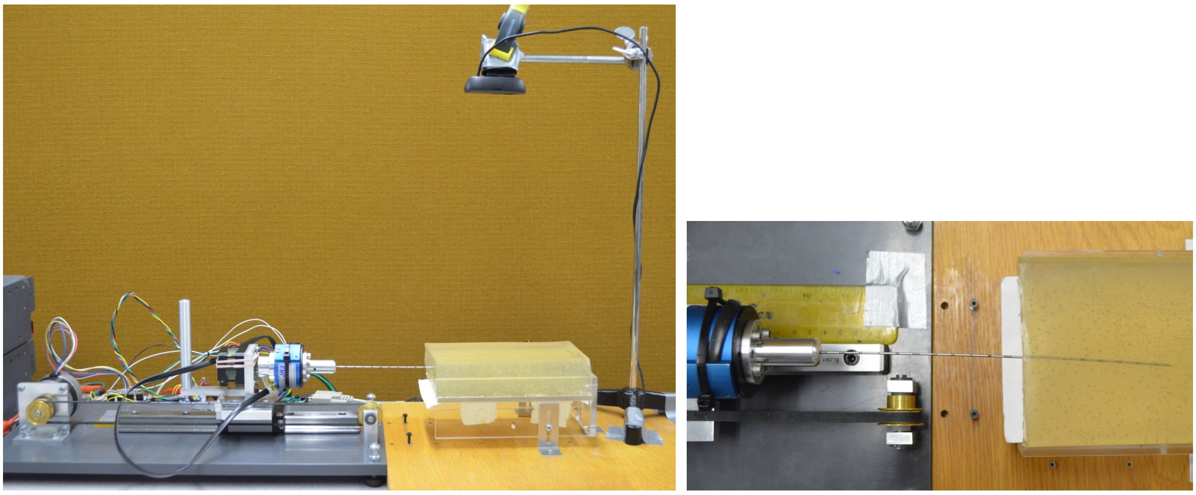

(a) (b)

Figure 4.5.: The experimental setup for needle insertion into soft tissue.

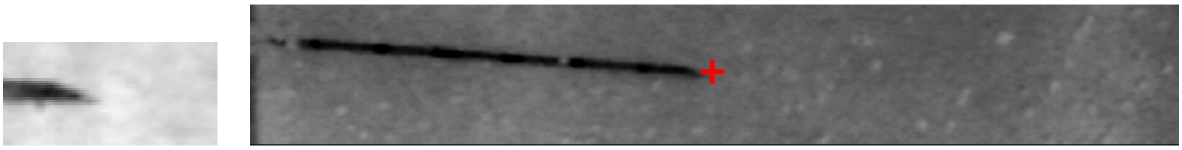

(a) The template used for tracking the needle tip.

(b) Tracked needle tip, indicated by the red cross at the tip.

Figure 4.6.: Needle deflection measurement via image processing.

tissue layer were too thin, the friction force along the needle would cause the tissue to be pushed back and distort the experimental results. A key factor of the phantom tissue is its transparency, since the needle needs to be tracked while being inserted in order to measure its deflection.

In order to determine the deflection, images of the needle inside tissue are recorded from above by a Logitech C270 web-cam during insertion. Since the needle deflection can only be monitored in the horizontal two dimensional plane, the deflection also needs to be kept to this plane. This can be achieved by aligning the bevel vertically. This way it can be safely assumed that the needle will deflect in the horizontal plane only. Potentially occurring gravity affects, which could lead to deflection in the vertical plane can be neglected as the magnitude is below the range of the sensor. Furthermore, the supporting effect of the tissue prevents the needle from being pulled down by gravity.

To track the needle tip during insertion for comparison to estimated deflection, template matching is was applied. The template is illustrated in Figure 4.6a. A MATLAB implementation by *Dirk-Jan Kroon* is used. The chosen matching method is normalized cross correlation (NCC). This approach provides a high robustness against brightness variations and specifically bubbles in the tissue (see Figure 4.6b, bright spots on the needle). The images have a resolution of 800 × 448 pixels and the camera observes a width of 80 mm at the height of the needle. This results in a resolution of 0.179 mm/pixel. The deflection is measured in respect to the unbent needle in air. It should be noted that image processing for measuring the needle tip deflection is only used for later comparison with model estimations and not for estimating the deflection itself.

The used needle is a standard 18G brachytherapy needle with an outer diameter of 1.27 mm and inner diameter of 1 mm. The bevel angle is roughly 20°. The length of the needle is 20 cm, but since a small part of the needle is clamped in the holder, the effective needle length, which can bend, is 19.1 cm.

4.2.1. Processing Data and Calculating Deflection

After recording, the relevant force, moment and image data are extracted from the recorded data. Only one of the three recorded dimensions for force and torque is needed, since the deflection is restricted to a two dimensional plane. To reassign the measured moments to the tip of the needle clamp, the moments are recalculated as described in Section 3.3.3. The images are then processed by using the described image processing algorithms to acquire the actual needle tip deflection. Listing 4.1 shows Matlab code of how the Young's Modulus (E) and Area Moment of Inertia (I) are calculated. Also the effective length of the needle, defined as `l` is shown (see line 7, Listing 4.1). Listing 4.2 and Listing 4.3 depict the model code for Abolhassani et al.'s and the proposed model, respectively. SI-units are used to calculate the deflection. The deflection values are finally recalculated to millimetres. The variables `F` and `M` represent the force and recalculated torque vector recordings from the sensor and `v` designates the tip deflection.

Listing 4.1: Matlab code for calculating the necessary needle parameters.

```
1 E = 200e9;          %Young's modulus [GPa] G=1e9, Pa = kg/(m*s^2)

3 r2 = 1.27e-3 / 2;   %Outer needle radius (needle packing) [m]
  r1 = 1e-3 / 2;      %Inner needle radius (wikipedia, 18G needle) [m]
5 I = pi*((r1+r2)/2)^3*(r2-r1);

7 l = 0.191; % length of needle [m] (20 cm - length inside adapter)
```

Listing 4.2: MATLAB code for Abolhassani et al.'s model

```matlab
for i=1:1:length(t)-1   %For all samples minus last sample
    dF = F(i+1)-F(i);
    dM = M(i+1)-M(i);
    dv = (3*dM*l^2-dF*l^3) / (6*E*I); %Deflection change between i-th and i+1-th sample
    v(i+1) = v(i) + dv; %Deflection
end

v = v.*1000;  %Recalculating to [mm]
```

Listing 4.3: MATLAB code for the proposed model

```matlab
l_in_0 = .01; %Pre-inserted part of needle [m]

l_in = t.*(speed/1000) + l_in_0; %Traveled distance in [m]
l_out = l - l_in;
a = 1/3;
b = 2/3;
a_1 = l_out+l_in*a;
a_2 = l_out+l_in*b;
F2 = (-M + F.* a_1)./(l_in.*(b-a));
F1 = F + F2;

v = (F1.*a_1.^2.*(3*l-a_1) - F2.*a_2.^2.*(3*l-a_2))/(6*E*I);

v = v.*1000;  %Recalculating to [mm]
```

4.3. Model Validation

To validate the introduced deflection model, the measured deflection is compared to the model estimation. In order to show that this model marks an improvement over previous deflection models, the model will be compared to the model proposed by Abolhassani et al. [9]. The insertion experiments are explained and the results of the validation experiments are shown.

4.3.1. Insertion Experiments

To verify the developed deflection model, insertion experiments were conducted consisting of six trials. Manual insertions with varying velocities and automated insertion with 10 mm/s and 15 mm/s were performed with two homogeneous tissue samples, which varied in stiffness. For this set of experiments, the needle was not turned at any point during the insertion and deflection was kept to the horizontal plane. The reasons for this are explained in section 4.2. Forces and moments at the needle base and images were recorded during the insertion. The insertion depth was 120 mm throughout all trials. Each trial consisted of 6 runs, in each of which a new point of insertion was used and

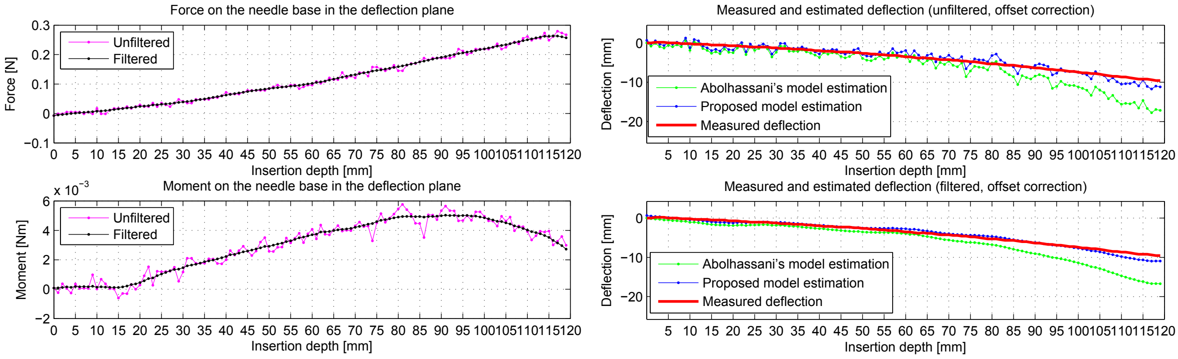

(a) Forces and moments acting at the needle base. (b) Measured (unfiltered) and estimated needle tip deflection.

Figure 4.7.: Sample plots for forces and moments at the needle base and tip deflection during insertion into tissue 1 with a velocity of 10 mm/s.

the needle bevel was adjusted to deflect into the right direction as seen from the side of the robot. The forces and moments were recorded during the insertion and used to estimate the deflection off-line. The measured tip deflection was finally compared to the estimated tip deflection.
For the manual insertion it was tried to keep the velocity at a constant level, since the insertion speed was not measurable in real-time. Before the start of insertion, the needle was inserted approximately 10 mm into the tissue for all trials. The used sampling rate for all trials was 10Hz to ensure that no ticks are missed and data recording is done in real-time. The image data was also recorded with the same sampling rate.

For these experiments, the Simulink model shown in Figure C.1 of the appendix was used. In the model, raw data from the force/torque sensor and image data are read. Also, the rotary speed of the carriage motor shaft is set to the appropriate level for the desired amount of time. The desired insertion depth and velocity can directly be chosen as well as a period of time for which data recording should be maintained after insertion is stopped.

4.3.2. Validation Results

Figure 4.7a shows a sample deflection curve of the needle tip (see Figure 4.7a) and forces and moments at the needle base during insertion (see Figure 4.7). The sensor data was filtered off-line by a zero-phase low-pass filter, using MATLAB's *filtfilt()* function. Figure 4.7 also shows the deflections estimated by a model proposed by Abolhassani et al.

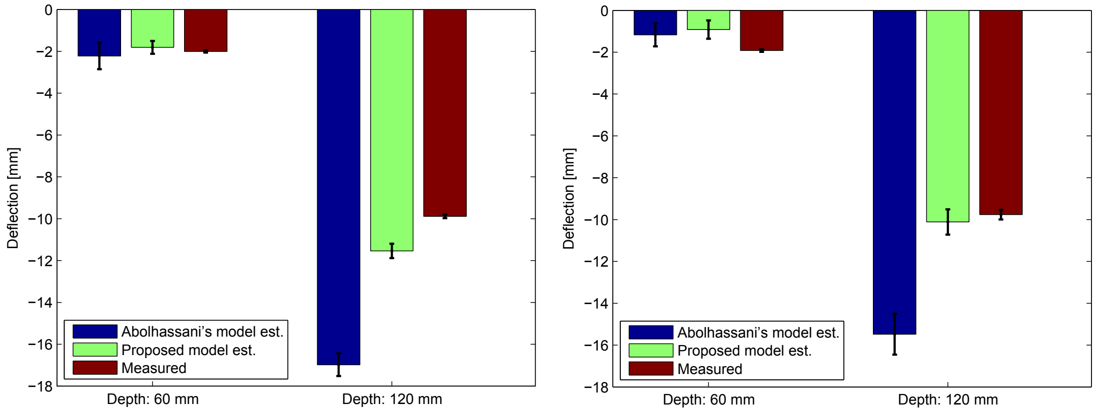

(a) Tissue 1 with velocity 10 mm/s.

(b) Tissue 1 with velocity 15 mm/s.

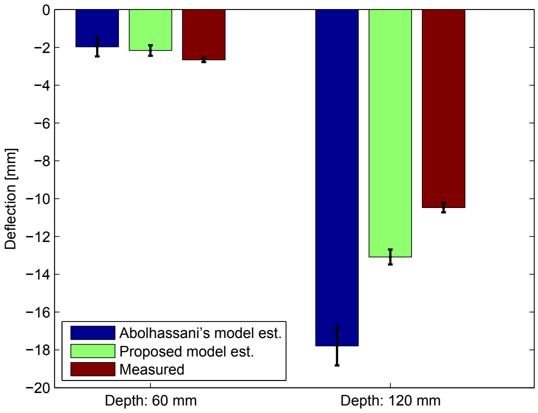

(c) Tissue 1 with manual insertion.

Figure 4.8.: Measured and estimated tip deflection with tissue 1. The error bars show the standard deviation ($n = 6$).

[10] and the estimation of our proposed model. As the plot shows, the estimations of both models are for small insertion depths very similar. At a depth of approximately 60 mm however, Abolhassani et al.'s model increasingly overestimates the deflection while the proposed model maintains a relatively high precision. In order to show that the mentioned discrepancy between the proposed model and Abolhassani et al.'s model persists throughout all carried out trials, the mean values of the six runs of each trial ($n = 6$) were calculated at the depths of 60 mm and 120 mm. The mean deflection at the chosen depths are plotted as groups of three bars in separate plots for each insertion trial. In Figures 4.8 and 4.9, the mean estimations and measurements ($n = 6$) at insertion depths of 60 mm and 120 mm are illustrated for the three trials of tissue 1 and 2 respectively. The data shows that the aforementioned overestimation later on during the insertion can be observed throughout all the trials. It furthermore shows

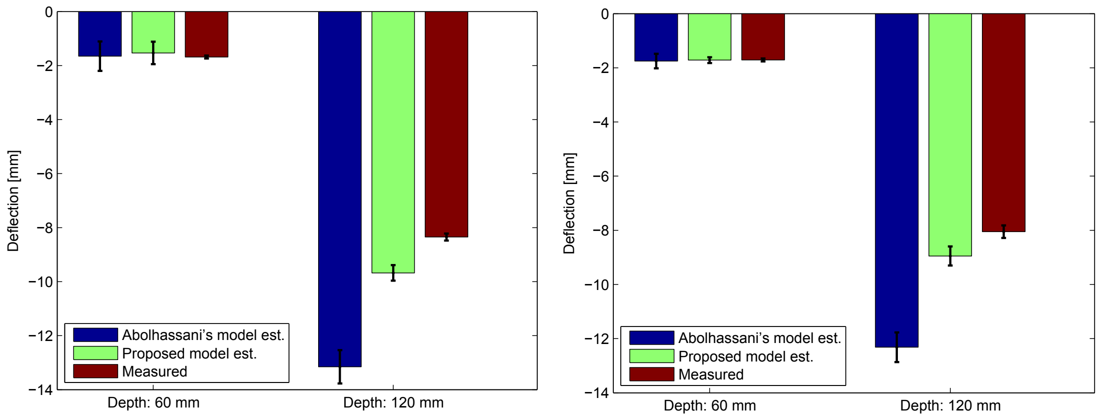

(a) Tissue 2 with velocity 10 mm/s.

(b) Tissue 2 with velocity 15 mm/s.

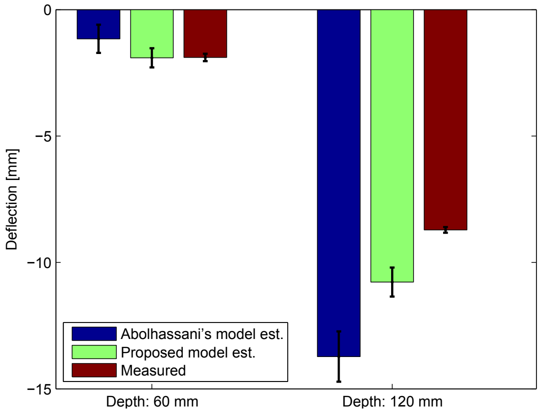

(c) Tissue 2 with manual insertion.

Figure 4.9.: Measured and estimated tip deflection with tissue 2. The error bars show the standard deviation ($n = 6$).

that the proposed model also slightly overestimates the deflection at a depth of 120 mm. At a depth of 60 mm, the estimations of both models are very close to the measured deflection throughout most of the trials.

In Figure 4.8b, which shows an insertion speed of 15 mm/s into tissue one, the mean value at 60 mm insertion depth shows that both models are underestimating. Since both models show a similar estimation error, it can be assumed that the reason for the wrong estimation is not a model error. The error could be due to the choice of insertion points into the phantom tissue. In this particular trial (15 mm/s and tissue 1), the chosen insertion point was at a relatively high position of the tissue samples' vertical cross-section. This could have changed the boundary conditions. The fact that this underestimation does not occur with tissue 2 and the same insertion velocity (see Figure 4.9b) also supports this assumption.

Table 4.1.: Results of a paired t-test performed on estimated and measured data.

Model		Tissue 1			Tissue 2		
		10^{a}	15	man	10	15	man
Abl[b] 60[c]	result	$\overline{r}^{d}$	$\overline{r}$	$\overline{r}$	$\overline{r}$	$\overline{r}$	$\overline{r}$
	p-val	0.758	0.256	0.283	0.960	0.903	0.278
Prp 60	result	$\overline{r}$	$\overline{r}$	$\overline{r}$	$\overline{r}$	$\overline{r}$	$\overline{r}$
	p-val	0.567	0.098	0.170	0.735	0.972	0.972
Abl 120	result	r	r	r	r	r	r
	p-val	5.5×10^{-5}	0.001	7.1×10^{-4}	0.001	4.4×10^{-4}	0.004
Prp 120	result	r	$\overline{r}$	r	r	r	r
	p-val	0.003	0.484	6.1×10^{-4}	0.023	0.047	0.012

---

[a] Insertion speed in *mm/s* or "man" for manual

[b] Model identifier, “Abl” for Abolhassani, “Prp” for proposed

[c] Insertion depth in *mm*

[d] "$\overline{r}$" if null hypothesis is *not* rejected

To show where the estimations are in fact significantly different to the measured deflection, a paired t-test was carried out using MATLAB’s function *ttest()*. The null hypothesis of a paired t-test is that the mean of the difference of two data sets is *not* significantly different. The significance level was chosen to be 5% ($\alpha = 0.05$), as this increases the significance of the test results compared to a smaller α. The test was carried out between measured and estimated samples ($n = 6$) for each model, for each trial and for the two observed insertion depths separately. The results of the t-test can be found in Table 4.1. They show that at the depth of 60 mm, all trials do not reject the null hypothesis, which means that both model estimations are not significantly different at this point. At the depth of 120 mm however, the test shows that both model estimations are significantly different from the measured deflection for most cases. Although no t-test was carried out between the two model estimations, it can clearly be observed that the estimations of the proposed model and Abolhassani et al.’s model are significantly different. The standard deviations do not overlap in any of the trials at a depth of 120 mm. This is specifically pointed out to illustrate the marked improvement of the proposed model over Abolhassani et al.’s model.

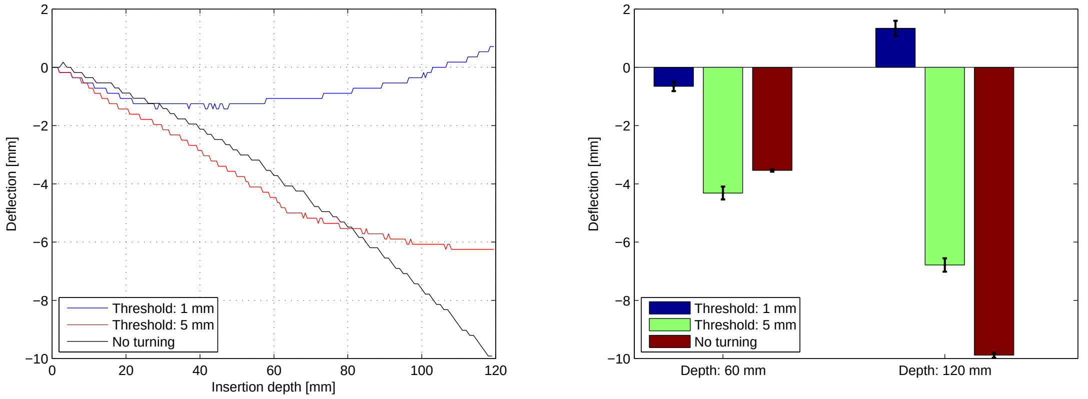

(a) Sample plot of the tip deflection.

(b) Average over 6 trials. The error bars show the standard deviation.

Figure 4.10.: The impact of needle turning about 180° at multiple deflection thresholds.

4.4. Correction of Deflection

A second type of experiment was performed to study the corrective effect of turning the needle about 180° when a certain estimated deflection threshold is reached. The needle is turned with an angular velocity of 180 deg/s. As the needle is being turned, the insertion is not paused but continues at the same speed. To estimate the threshold, the virtual sensor, which utilizes the developed model, was used. Two trials were executed, also consisting of six runs each. In each trial the threshold was set to a different level, the first being 1 mm and the second 5 mm. The needle also deflected in each run to the right side, or negative y-direction, until it was turned. One of the tissue samples, which was used for the first experiment (tissue 1) was used for this set of experiments. The runs involving turning the needle were conducted with a velocity of 5 mm/s and for the comparison with deflection without turning, data from the model verification experiment was used. Although the speed differs in between the experiments from 5 to 10 mm/s, judging by Figure 4.8 and Figure 4.9, the insertion velocity does not influence the amount of deflection. This was also concluded by Webster et al. in 2005 [26].

For this set of trials, the Simulink model depicted in Figure C.3 of the appendix was used. This model essentially has the same capabilities as the model used for simpler insertion experiments without rotation (see Figure C.1). Additional capabilities are the on-line calculation of the needle tip deflection during insertion, a necessary average filter and offset correction for force/moment data, and a trigger function for needle rotation

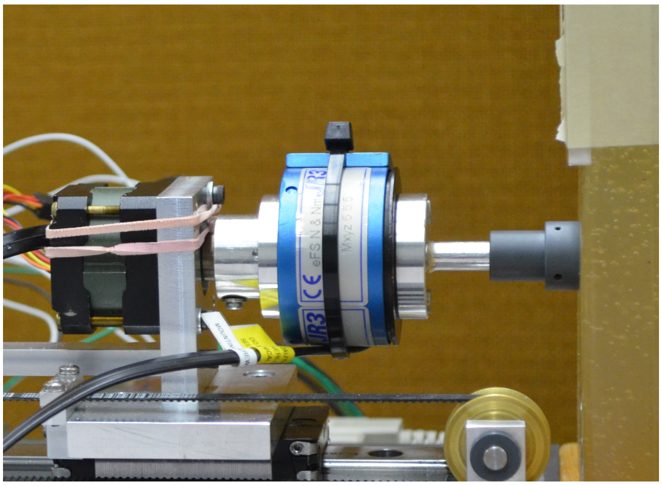

Figure 4.11.: The setup for the tissue indentation tests.

about 180° when a set threshold is reached. All the described block functions can be found in the toolkit library shown in Figure C.2 of the appendix.

On-line force readings are used to estimate the deflection with the proposed model in real-time. Figure 4.10a shows three insertions: one without rotation, rotated at 5 mm deflection threshold and one rotated at 1 mm deflection threshold. The plot shows that turning the needle at a specific point has a very noticeable impact on the deflection. According to Figure 4.10a, the best point for turning the needle is relatively early. The best correction results are achieved when the needle is turned when 1 mm deflection is reached. Figure 4.10b reaffirms this claim. Here the mean ($n = 6$) of each trial (turning at 1 mm, 5 mm and not turning) is shown for an insertion depth of 60 and 120 mm. The error bars, which show the standard deviation, indicate that the results for each turning point are significantly different. None of the error bars overlap.

4.5. Tissue Stiffness Measurement

A third experiment was carried out to determine the stiffness of the tissue samples used in the first two experiments via indentation. Figure 4.11 shows the experimental setup. Purpose of this experiment's results is to show how much the tissue samples differ in stiffness and also to quantify the tissue stiffness. It should also show that there is a *noticeable* difference in stiffness for the two tissues and this way verify that sufficient variance in stiffness was given for the validation experiments of the deflection model.

Three indentation trials were conducted for each tissue sample with 4 mm, 8 mm and 12 mm of depth and a velocity of 1 mm/s for each run. The diameter of the used stamp

Table 4.2.: Results of the indentation tests.

	Tissue 1			Tissue 2		
	4^a	8	12	4	8	12
k^b	0.383	0.379	0.387	0.288	0.262	0.262
${\sigma_k}^c$	0.035	0.006	0.013	0.023	0.016	0.008
mk^d		0.383			0.271	
F^e	1.53	3.03	4.64	1.15	2.09	3.15
σ_F	0.142	0.051	0.155	0.091	0.131	0.101

---

[a] Indentation depth in mm
[b] $k = \frac{F}{\text{indent depth}}\ [\frac{N}{mm}]$
[c] Standard deviation
[d] Mean of k
[e] Force in N

was 19.05 mm. Each trial consisted of 6 runs. The forces in z-direction were recorded during indentation and for two seconds after the indentation depth was reached. The recorded force data during two seconds after indentation was averaged. This average was used to determine the stiffness

$$k = \frac{F}{x} \tag{4.13}$$

of each run where F is the force average after 2 s of maximum indentation depth and x is the maximum indentation depth for the trial. The mean of the stiffnesses of each run ($n = 6$) and the mean of all three trials for each tissue was then determined. Table 4.2 shows the results of the indentation test.

5. Utilizing a Sensorized Template

In case the design of an assisting robotic system demands the inclusion of a template, the forces and moments occurring during needle insertion can not be measured adequately at the needle base, because forces/moments caused by needle deflection are absorbed at the template. Hence, the forces and moments must be measured at the template. In this chapter, necessary adjustments to the deflection model and the experimental setup for testing a sensorized template will be explained. Moreover, the experimental results will be presented. It shall be shown to which extent force and moment measurements at the template were possible with the used experimental setup.

5.1. Model Adjustment

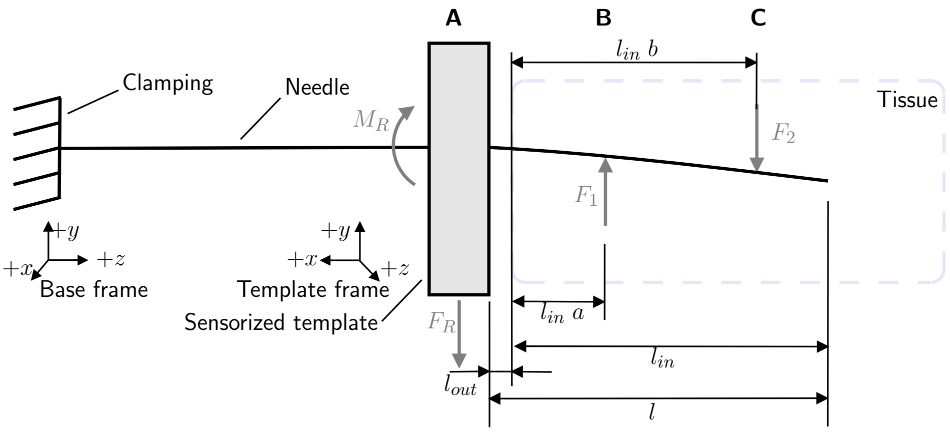

Figure 5.1.: A diagram of the forces and moments acting on needle and sensorized template.

It is assumed that the previously introduced model can be adjusted to calculate the deflection when measuring forces and moments at the template. In this case, the portion of the needle, which is prone to bend, is not static as opposed to a setup without template. It increases as the needle is being inserted into tissue. This variable needle

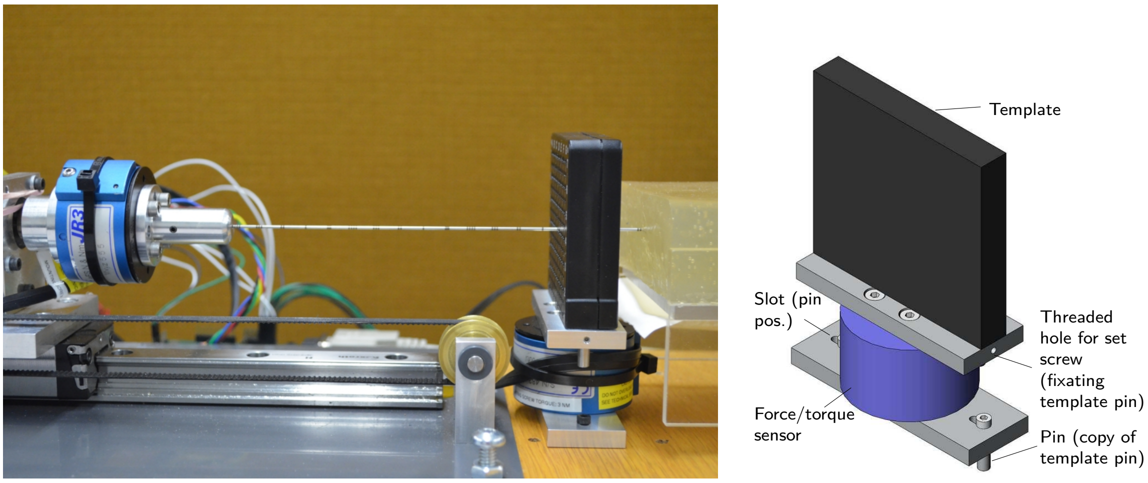

(a) The experimental setup. (b) The sensorized template.

Figure 5.2.: The setup for conducting insertion experiments with a sensorized template.

length is measured from the right side of the template to the needle tip. The forces and moments acting on needle and template and the necessary dimensions used in the altered deflection model are illustrated in Figure 5.1. The altered model would theoretically be valid with the assumptions that the force (F_R) and moment (M_R) can be measured on the template as shown in Figure 5.1 and naturally have a similar progression as without a template, which means the directions of force F_R and moment M_R should be equal. The tip deflection $\delta_{1,2}$ changes to

$$\begin{aligned}\delta_{1,2} =& \frac{F_1\ (l_{out}+l_{in}\ a)^2\ (3l-l_{out}-l_{in}\ a)}{6EI} \\ &- \frac{F_2\ (l_{out}+l_{in}\ b)^2\ (3l-l_{out}-l_{in}\ b)}{6EI}\end{aligned} \tag{5.1}$$

where l is the variable length of the needle, which is subject to bending. The change of the length depends on and is equal to the insertion speed. The only difference from (5.1) to (4.8) is the variable length l. The equations for F_1 and F_2 ((4.11) and (4.12)) remain unchanged.

5.2. Experiments

Four runs of insertion experiments were performed with and without the use of a template. A constant insertion velocity of 10 mm/s was maintained until a depth of 115 mm was reached. The same tissue was used for all eight runs. In each run, a new insertion

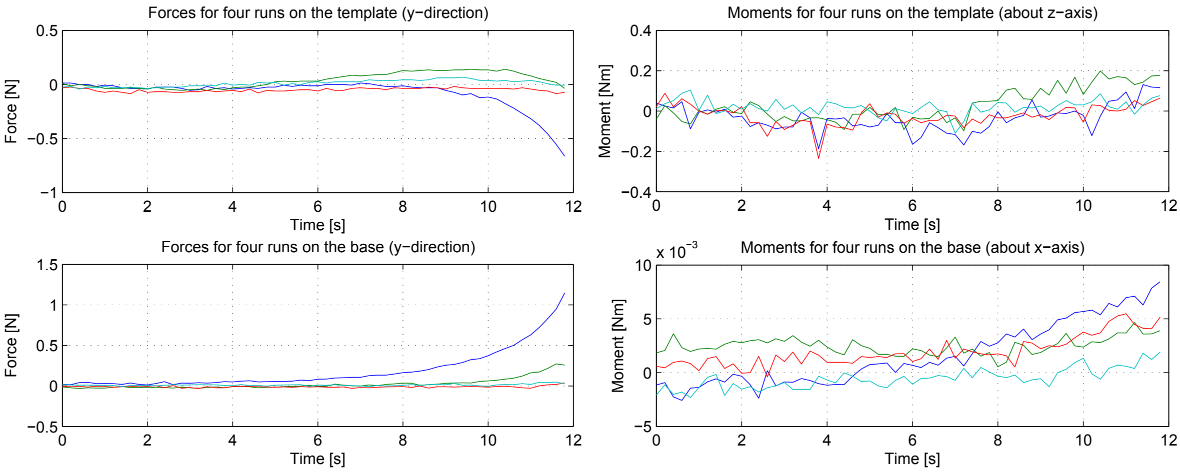

(a) Forces acting on the template during insertion.

(b) Moments acting on the template during insertion.

Figure 5.3.: Forces (in y-direction) and moments (about z-axis) acting on the sensorized template. Each curve shows the force or moment progression for a separate run.

point in the tissue was chosen or a different hole in the template, which also results in a different insertion spot.

For the experiments involving a template, it is of vital importance that the needle base is at the centre of the intended template hole for insertion. If this is not the case, the needle is bent by the template during insertion and thus exerts a force onto the template, which can be observed as a force at both the template and base sensors. This force, which acts as an interference, must be avoided by centring the needle inside the template hole before inserting it into tissue. Since the assistant system and tissue ground plate could only be moved relatively coarsely, precisely centring the needle was hardly possible. In order to measure any interfering forces beforehand, the needle was first only inserted into the template without placing tissue after the template. The recorded forces and moments at the base and template were afterwards deducted from the insertion with tissue. It was presumed that the aforementioned interfering forces would be cancelled out by this measure.

5.2.1. Experimental Setup

The experimental setup for conducting needle insertions with a template includes a template of the same type, which is used in brachytherapy procedures. Attached to the

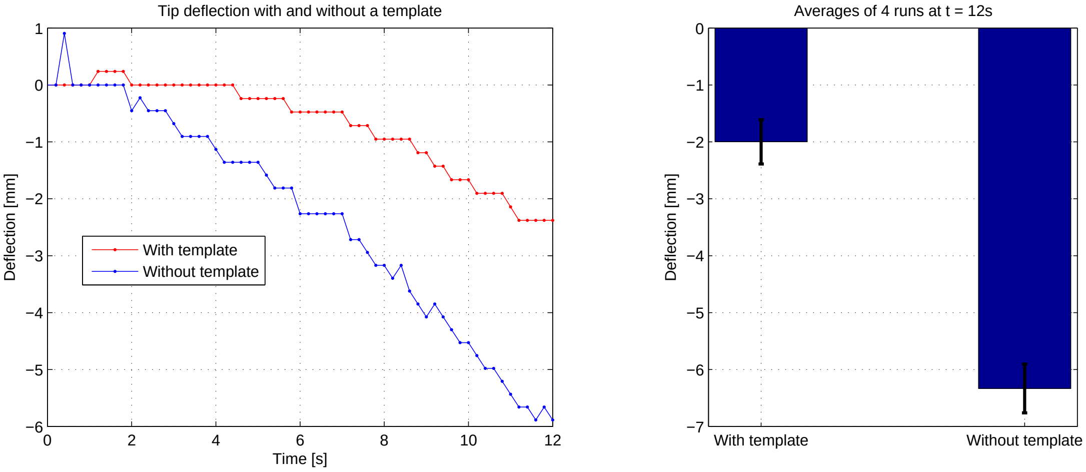

(a) Sample plot of deflection with template vs. without template.

(b) Mean of four runs with vs. without template.

Figure 5.4.: Deflection for insertions with vs. without template.

template is a force sensor of type (JR3 50M31A-I25), which is the same sensor used for measuring forces/moments at the needle base. The template sensor is fixed to the same wooden plate (see Figure 5.2a), to which the tissue stand is attached. Figure 5.2a shows a close-up view of the experimental setup and Figure 5.2b shows a CAD model of the sensorized template. The plate below the template sensor (see Figure 5.2b) is a copy of the template's bottom side with the same pin measures as the template's pins. The pin distance of the bottom plate can be adjusted to fit the holes in the wooden ground plate. The axes of the template sensor were aligned such that the magnitude and direction of the deflection force are measured along the same axis for both sensors (see Figure 5.1). Forces and moments at the needle base and the template are measured on order to monitor to which extent forces/moments are absorbed by the template. The distance between template and tissue was 22 mm.

5.3. Results

When comparing the recorded template forces/moments during insertion, it was revealed that the recordings of each run show hardly any similarities. Figure 5.3 shows the forces and moments for four runs. There is no significant trend or a similar progression, which all the data sets have in common. The occurrence of a sudden rise in forces and moments at the needle base towards the end of insertion is an indicator for the needle not being placed in the centre of the template hole. If the needle had been precisely adjusted to the centre of the used template hole, there should be hardly any noticeable forces occurring at the needle base. Consequently it does not make sense to apply the alternated deflection model to the recorded data. The inconsistency of the data means that it is virtually impossible to precisely centre the needle to the template with the current setup and that it is therefore not possible to measure deflection forces and moments at the template accurately. Another reason for inaccurate force readings can be a bent needle. A slight bend or a small dent in a needle would be sufficient to alter the force/moment readings during insertion.

A more accurate statement can be made about the difference in deflection when a template is used. Figure 5.4 shows how the template has a decreasing effect on the needle deflection. Figure 5.4a illustrates the trajectory of the needle tip during insertion into tissue with and without a template. It can be observed that the use of a template decreases the deflection drastically about 50% at a final depth of 115 mm. Figure 5.4b confirms this statement. It shows the mean deflection ($n = 4$) at 115 mm for experiments with both including and not including a template.

In (5.1), it can be seen that the magnitude of l has a direct impact on the amount of tip deflection. It directly contributes to a lower amount of deflection at an early stage of insertion. Hence, the increase of tip deflection is lessened at an early stage of insertion compared to deflection without a template.

6. Discussion

This chapter discusses and reiterates necessary future improvements to the assistant system, which is described in Chapter 3. Furthermore, the virtual deflection sensor, which is introduced in Chapter 4, is discussed including the deflection model's strengths, weaknesses and possible improvements. Subsequently, the usability of the sensorized template explained in Chapter 5 is debated. Finally, the necessary future steps are named.

6.1. Surgeon's Assistant Prototype

Although the system in the presented state is sufficient to conduct needle insertion experiments, there are some aspects, which require improvement. One aspect is the maximally admissible sampling rate, which needs to be drastically improved in the future, since a maximum sampling rate of 20Hz is very restrictive. Increasing the sampling rate can be achieved by either using a different DAQ card or a different force sensor, which offers a better compatibility with the HILINK board. For a DAQ card alternative, a Quanser DAQ card could be considered. The Quanser cards are also interfaced via Simulink using the QuaRC software package, which provides a much larger block library. Although the QuaRC software also runs in soft real-time, the performance is much higher [5]. The JR3 force sensor is also supported, which means the currently used force sensor can be included seamlessly into Simulink models, which control the motors. In case a force sensor alternative is considered, an analogue sensor could be used, which can establish a direct connection to the analogue inputs of the HILINK board. This would enable to run the HILINK board in hard real-time mode, which would lead to a drastically increased sampling performance.

Due to the relatively high range of the currently used force sensor, using a different sensor with a lower range should be considered. The used JR3 sensor is very close to its lower limit, especially for measured moments. The results (cf. Section 4.3.2) show that the maximally occurring forces at the needle base are in the sub-Newton range (see Figure 4.7a). Therefore, the sensor's range should be in the order of ten and even lower for moments. Details about the force sensor's specifications are given in Section B.3 of the appendix.

Further considerations are necessary for the motors used in the system. Replacing the stepper motors for carriage control and needle rotation with DC motors would significantly lower the limit of position resolution. Furthermore, DC motors are not prone to vibration, which would eliminate currently induced frequencies by the stepper motors. This would also enable smoother motions, especially for low velocities. DC motors would further lift the restriction of decreasing torque with higher rotational speeds.

Lastly, a linear encoder would be needed to determine the position of the carriage. This is particularly important for manual insertion, where so far the position of the carriage and hence the insertion progress can not be determined via software. A DC motor's rotary encoder could not be used since the motor is disconnected for manual insertion. An alternative to a linear encoder would be an optical tracking system to track the carriage and thus needle motion.

6.2. Virtual Deflection Sensor

The distribution of the loads described in Section 4.1, which are applied by the tissue onto the needle, are an assumption, as previously mentioned. Further investigation would be necessary to examine whether the load distribution is triangular or has a rather different shape. If the shape is in fact different, the factors a and b in (4.8)(see also Figure 4.2a) can be adjusted to fit the load distribution. The parameters a and b could also be fit to measured data in order to obtain a higher precision for the effective position of F_1 and F_2. This could further improve the model's performance, especially as the insertion depth increases.

Figure 6.1 shows the trend of the needle base force during insertion. Especially the rapid decline of the force from 13 seconds onwards is notable. Considering the model description, the force should not decrease after the insertion is stopped; it should rather stay the same from this point on. The fact that the forces do decrease might indicate that the occurrence of the distributed loads (q_1 and q_2) explained in Section 4.1 occur due to the component of friction forces perpendicular to the longitudinal needle axis in y-direction (cf. Figure 4.2a). This would, however, not mean that the proposed

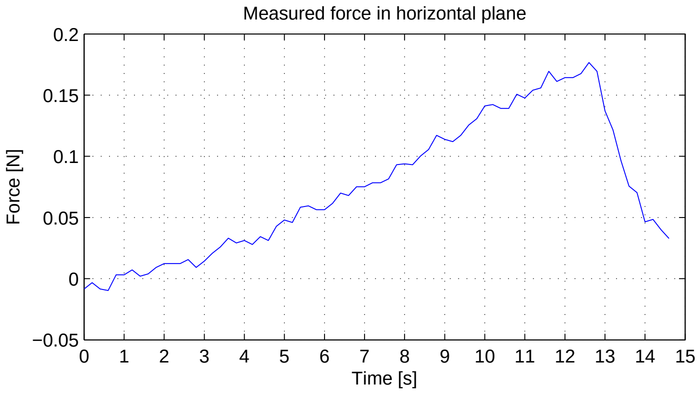

Figure 6.1.: Force trend at the needle base during needle insertion. The insertion depth is approximately 130 mm and insertion speed is 10 mm/s. The insertion was stopped after 13 seconds.

model is invalid. The distributed loads would still exist and still remain valid, since the model has been successfully validated. The reason for their existence would merely be different from how they are explained in Section 4.1. Particularly for manual insertion, where the surgeon could pause insertion and then resume, it would be crucial to find the actual cause of the distributed loads q_1 and q_2, such that the needle deflection can reliably be estimated in such a scenario. Also, a more accurate load distribution than the proposed triangular distribution could be found by further investigating the cause of the distributed loads.

Furthermore, it should be noted that the model can only estimate the deflection while the needle has not been turned. After the needle is turned, the distributed loads along the needle change.

6.3. Sensorized Template

In order to conduct needle insertion experiments, which include a template, a means of precisely centring the needle in a template hole is necessary. Therefore, the assistant system should be mounted on a translational stage, which allows for it to be shifted into two directions: horizontally, perpendicular to the needle axis, and vertically. To adjust the position of the assistant with sufficient precision, a resolution in the range of 1/10 to 1/100 mm would presumably be necessary. This modification would also extend the assistant system to a four DOF system. The extension would in fact also be necessary for a setup without a template, as the insertion point needs to be adjusted according to the position of insertion in horizontal and vertical direction.

Since the forces occurring perpendicular to the needle axis during insertion are very small and a very high precision of needle positioning before insertion is necessary, relying solely on force/moment measurement at the template is not recommended at this point. Too many uncertainties and sources of errors make this type of deflection measurement rather inconsistent and therefore unsafe. Once a more advanced version of the assistant system is available, this approach should be tested more thoroughly. With the appropriate amount of precision, the results would likely improve.

If the incorporation of a template is not further pursued, the template would have to be completely abandoned because otherwise a virtual sensor, which relies on force/moment measurement at the base, could not function. The template could in the future be replaced by a mechanism, which initially provides needle guidance until the needle has poked through the patient's skin. From this point on, the mechanism could be retracted such that deflection forces can be measured at the base while further inserting the needle.

6.4. Future Work

In order to further advance the surgeon's assistant system, the continuing work involves to advance the system's design, such that it can be mounted onto and used together with the equipment for brachytherapy procedures, such as the Brachystepper (see Figure 1.3). The existing system would likely have to be redesigned. While the basic system of a rail-guided carriage (see Figure A.3 of the appendix) could be further utilized, the PVC ground plate should be replaced with the in Section 6.3 mentioned two DOF translational stage. This stage, which would carry the rail-carriage system, would then be mounted onto the Brachystepper. These additions would effectively extend the overall assistant assembly to a four DOF robotic system. The two DOF translational stage would allow for the assistant system and thus the point of needle insertion on the tissue surface to be shifted horizontally and vertically. This would provide precise positioning of the needle to the desired seed placement location prior to insertion.

In the experiments for model validation (see Section 4.3), homogeneous tissue samples were used. In order to verify that the proposed deflection model will also maintain a high precision in inhomogeneous tissue, insertion experiments with such tissue need to be conducted. Furthermore, these phantom tissue samples should resemble the stiffness and inhomogeneities of real prostate tissue as closely as possible, in order to determine the precision of deflection estimation in prostate tissue.

Moreover, the setup should be expanded to measuring the needle deflection in the three dimensions to verify that the proposed model can be used in 3D space and not only the here tested 2D plane. To cover the vertical plane, a magnetic tracking or ultrasound imaging system might be necessary.

The in Section 6.2 mentioned necessary investigations to find an alternative cause for the distributed loads q_1 and q_2 are also a priority since this could further improve the deflection model.

The final proposition is to further investigate the usability of a sensorized template. In order to do this, as for force measurement at the needle base, a force sensor with a higher resolution is necessary. It should also be tested, whether the standard template, which is made out of plastic, is rigid enough to measure forces appropriately. For this purpose it might be necessary to design a more fitting template prototype in terms of rigidity for force measurements. Before further investigating force measurement at the template, the suggested advancements to the assistant system should be made to enable precise needle positioning.

7. Conclusion

In this work, a prototype of a robotic assistant system for prostate brachytherapy was introduced. The system is intended to support the surgeon and facilitate brachytherapy procedures by increasing the precision of seed placement. The setup of the system successfully performed needle insertion experiments with high precision and low maintenance. Although there are several improvements necessary, it is advanced enough to record force and moment data at the needle base for needle insertion experiments with different strategies such as manual and automated insertion. It provides a basic platform for needle insertion experiments, which should be further advanced. The modular design of the robotic system allows for alterations of single components without the need of rebuilding the entire setup. This provides flexibility and cost-efficiency for further design advancements.

The force sensor based virtual sensor, which is incorporated in the robotic system and based on mechanical properties of the needle, introduces a new approach as to how the forces are composed along the axis of the inserted needle into tissue. This new approach was proven to be more accurate than previously proposed mechanical deflection models. It is able to precisely sense the needle tip deflection during needle insertion procedures without relying on any other invasive or non-invasive devices than a 4 DOF force sensor, which measures the forces and moments at the needle base. Higher precisions can be maintained over higher insertion depths with the proposed model than other models before. Despite the good estimation performance of the mathematical model behind the virtual sensor, the reasoning behind the forces and moments, which act along the needle should be revisited and improvements made if necessary. This could contribute to further enhancement of the precision of deflection estimation. The virtual deflection sensor itself can not only be applied in prostate brachytherapy but a wide range of medical procedures, which involve needles prone to deflection.

It was furthermore shown that adjusting the bevel location during the insertion can drastically increase the tip targeting accuracy with only one rotation during insertion.

Limiting the amounts of needle rotation decreases tissue trauma and so further improves the procedure.

A further researched aspect was the usage of a sensorized template to measure force and moment data during insertion in order to estimate deflection. Since the results, however, showed conflicting measurements, the assistant assembly needs improvement in order to further advance this approach.

References

[1] Prostate Brachytherapy Center, 09 2012. URL `http://www.prostate.gr/gallery/en`.

[2] Prostate Brachytherapy info.net: Media Information Centre, 09 2012. URL `http://www.prostatebrachytherapyinfo.net/MED12.html`.

[3] McMaster-Carr, 10 2012. URL `http://www.mcmaster.com/#`.

[4] Unipolar Stepper Motor Driver Circuit - Northwestern Mechatronics Wiki, 10 2012. URL `http://hades.mech.northwestern.edu/index.php/Unipolar_Stepper_Motor_Driver_Circuit`.

[5] Quanser - control solutions - control software - WinCon, March 2013. URL `http://www.quanser.com/english/html/solutions/fs_soln_software_QuaRC.html`.

[6] Rexroth - ball rail systems, March 2013. URL `http://www.boschrexroth-us.com/country_units/america/united_states/sub_websites/brus_dcl/Products/Profiled_Rail_Systems/Ball_Rail_Systems/index.jsp`.

[7] Zeltom.com, 05 2013. URL `http://zeltom.com/products/hilink`.

[8] N. Abolhassani, R. Patel, and M. Moallem. Trajectory generation for robotic needle insertion in soft tissue. *Conf Proc IEEE Eng Med Biol Soc*, 4, 2004.

[9] N. Abolhassani, R. Patel, and F. Ayazi. Needle Control along Desired Tracks in Robotic Prostate Brachytherapy. In *Systems, Man and Cybernetics, 2007. ISIC. IEEE International Conference*, pages 3361 –3366, Oct. 2007. doi: 10.1109/ICSMC.2007.4413819.

[10] N. Abolhassani, R. Patel, and F. Ayazi. Minimization of needle deflection in robot-assisted percutaneous therapy. *Int J Med Robot*, 3(2):140–8, 2007.

[11] Niki Abolhassani and Rajni V Patel. Deflection of a Flexible Needle during Insertion into Soft Tissue. In *Proceedings of the 28th IEEE EMBS Annual International Conference*, volume 1, pages 3858–3861, August 2006. doi: 10.1109/IEMBS.2006.259519. PMID: 17946584.

[12] Niki Abolhassani, Rajni Patel, and Mehrdad Moallem. Experimental study of robotic needle insertion in soft tissue. *International Congress Series*, 1268:797 – 802, 2004. ISSN 0531-5131. doi: 10.1016/j.ics.2004.03.110. CARS 2004 - Computer Assisted Radiology and Surgery. Proceedings of the 18th International Congress and Exhibition.

[13] Ron Alterovitz, Andrew Lim, and Ken Goldberg. Steering flexible needles under markov motion uncertainty. In *Proc. IEEE/RSJ Int. Conf. on Intelligent Robots and Systems (IROS)*, pages 120–125, 2005.

[14] A. Asadian, M.R. Kermani, and R.V. Patel. An analytical model for deflection of flexible needles during needle insertion. In *Intelligent Robots and Systems (IROS), 2011 IEEE/RSJ International Conference on*, pages 2551–2556, 2011. doi: 10.1109/IROS.2011.6094959.

[15] Alain Gerbaulet, Richard Pötter, Jean-Jacques Mazeron, Harm Meertens, and Erik Van Limbergen. *The GEC ESTRO Handbook of Brachytherapy.* European Society for Therapeutic Radiology and Oncology, 2002.

[16] James M. Gere and Barry J. Goodno. *Mechanics of Materials.* CL Engineering, 2012. ISBN 1111577730.

[17] R.C. Hibbeler. *Engineering Mechanics: Statics.* Engineering Mechanics. Prentice Hall, 12 edition, 2010. ISBN 9780136077909.

[18] A. Jemal, F. Bray, M. M. Center, J. Ferlay, E. Ward, and D. Forman. *Global cancer statistics. CA: A Cancer Journal for Clinicians*, 61:69–90, 2011. doi: 10.3322/caac.20107.

[19] Hiroyuki Kataoka, Toshikatsu Washio, Michel Audette, and Kazuyuki Mizuhara. A Model for Relations Between Needle Deflection, Force, and Thickness on Needle Penetration. In *Medical Image Computing and Computer-Assisted Intervention - MICCAI 2001*, pages 966–974. Springer Berlin / Heidelberg, 2001. ISBN 978-3-540-42697-4.

[20] Hiroyuki Kataoka, Toshikatsu Washio, Kiyoyuki Chinzei, Kazuyuki Mizuhara, Christina Simone, and Allison M. Okamura. Measurement of the tip and friction force acting on a needle during penetration. In *Proceedings of the 5th International Conference on Medical Image Computing and Computer-Assisted Intervention-Part I*, MICCAI '02, pages 216–223, London, UK, UK, 2002. Springer-Verlag. ISBN 3-540-44224-3.

[21] V. Lagerburg, M.A. Moerland, J.J.W. Lagendijk, and J.J. Battermann. Measurement of prostate rotation during insertion of needles for brachytherapy. *Radiother Oncol*, 77(3):318–23, 2005.

[22] Thomas Lehmann, Mahdi Tavakoli, Nawaid Usmani, and Ronald Sloboda. Force Sensor Based Estimation of Needle Tip Deflection in Brachytherapy. *Journal of Sensors*, in press. doi: 10.1155/9161.

[23] Allison M Okamura, Christina Simone, and Mark D O'Leary. Force Modeling for Needle Insertion Into Soft Tissue. *IEEE Transactions on Bio-Medical Engineering*, 51(10):1707–16, October 2004. ISSN 0018-9294. doi: 10.1109/TBME.2004.831542.

[24] T K Podder, J Sherman, D Fuller, E M Messing, D J Rubens, J G Strang, R A Brasacchio, and Y Yu. In-vivo measurement of surgical needle intervention parameters: a pilot study. *Conf Proc IEEE Eng Med Biol Soc*, 1: 3652–5, 2006. ISSN 1557-170X. URL `http://www.biomedsearch.com/nih/In-vivo-measurement-surgical-needle/17946194.html`.

[25] R.S. Sloboda, N. Usmani, J. Pedersen, A. Murtha, N. Pervez, and D. Yee. Time course of prostatic edema post permanent seed implant determined by magnetic resonance imaging. *Brachytherapy*, 2010.

[26] R.J. Webster, J. Memisevic, and A.M. Okamura. Design Considerations for Robotic Needle Steering. In *Proceedings of the 2005 IEEE International Conference on Robotics and Automation, 2005. ICRA 2005*, pages 3588 – 3594, April 2005. doi: 10.1109/ROBOT.2005.1570666.

[27] Robert J. Webster, Jin Seob Kim, Noah J. Cowan, Gregory S. Chirikjian, and Allison M. Okamura. Nonholonomic modeling of needle steering. *Int. J. Rob. Res.*, 25(5-6):509–525, May 2006. ISSN 0278-3649. doi: 10.1177/0278364906065388.

Appendix A.

Mechanical Components

This chapter provides diagrams and a CAD model of the surgeon's assistant system from various perspectives. Figure A.1 and Figure A.2 provide a general overview over the initially planned system. The Figures schematically sketch the generally desired setup of the system, as it is intended to be used in prostate brachytherapy procedures. The difference between Figure A.1 and Figure A.2 lies in the second template, which is used to apply perpendicular pressure onto the needle shaft thereby providing one additional means of trajectory correction to the approach of needle turning in Figure A.1.

Figure A.3, Figure A.4 and Figure A.5 show the CAD model of the assistant system as it was built from three different perspectives. The parts coloured in brown and the PVC ground plate (see Figure A.3) represent parts, which were custom made by the department's machine shop in accordance with provided design specifications.

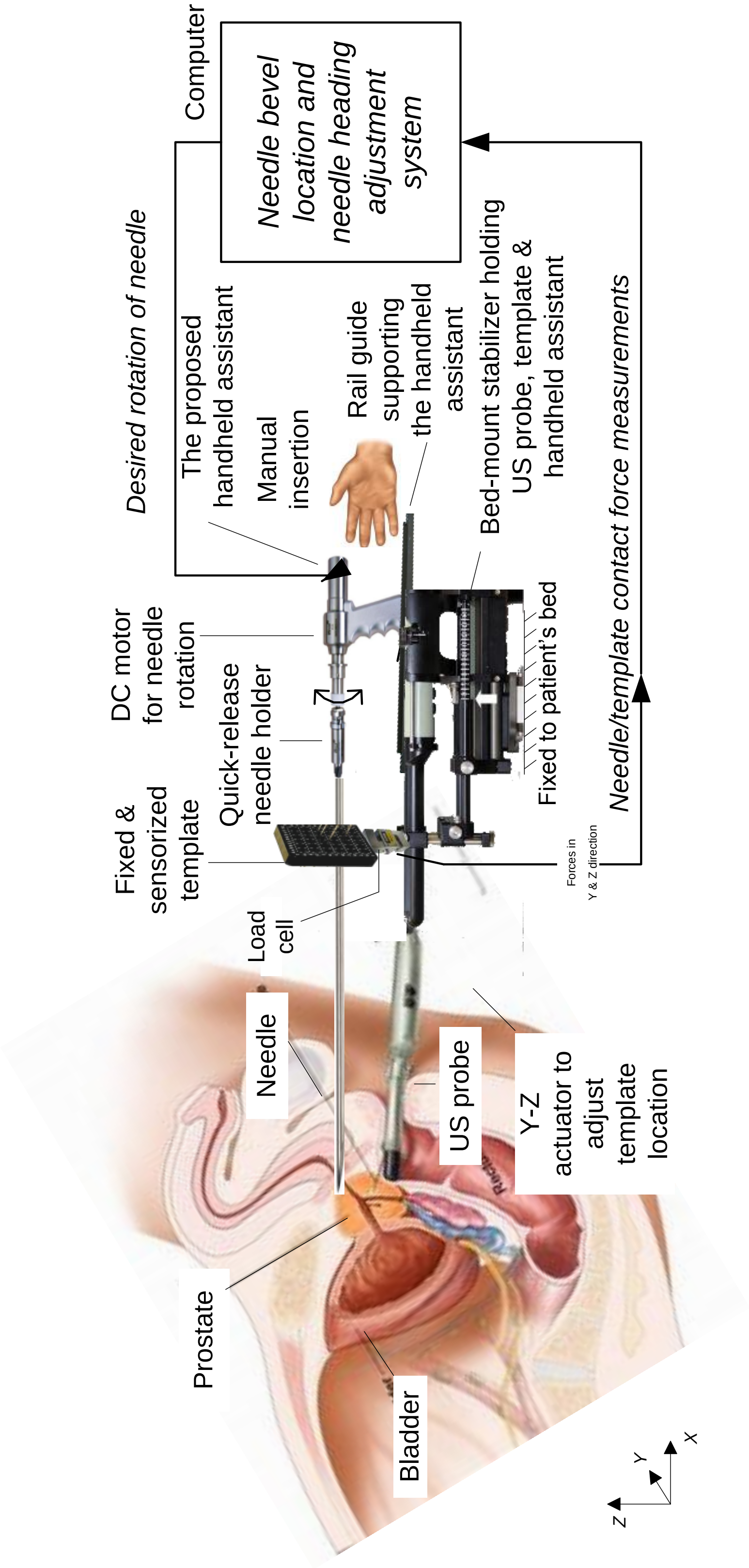

Figure A.1.: The first layout proposal of the assistant with only needle rotation for needle path correction.

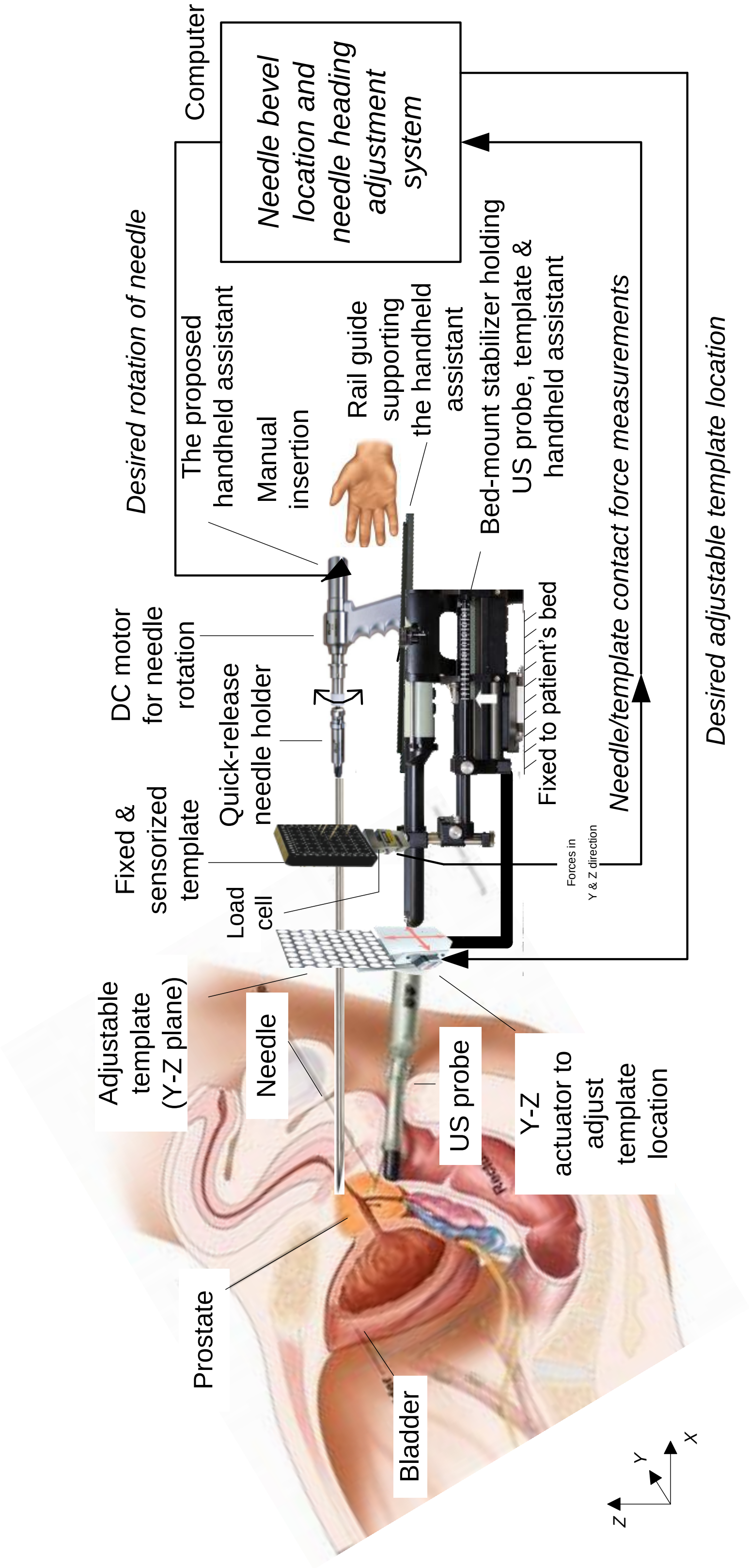

Figure A.2.: The first layout proposal of the assistant with both alternatives for needle path correction.

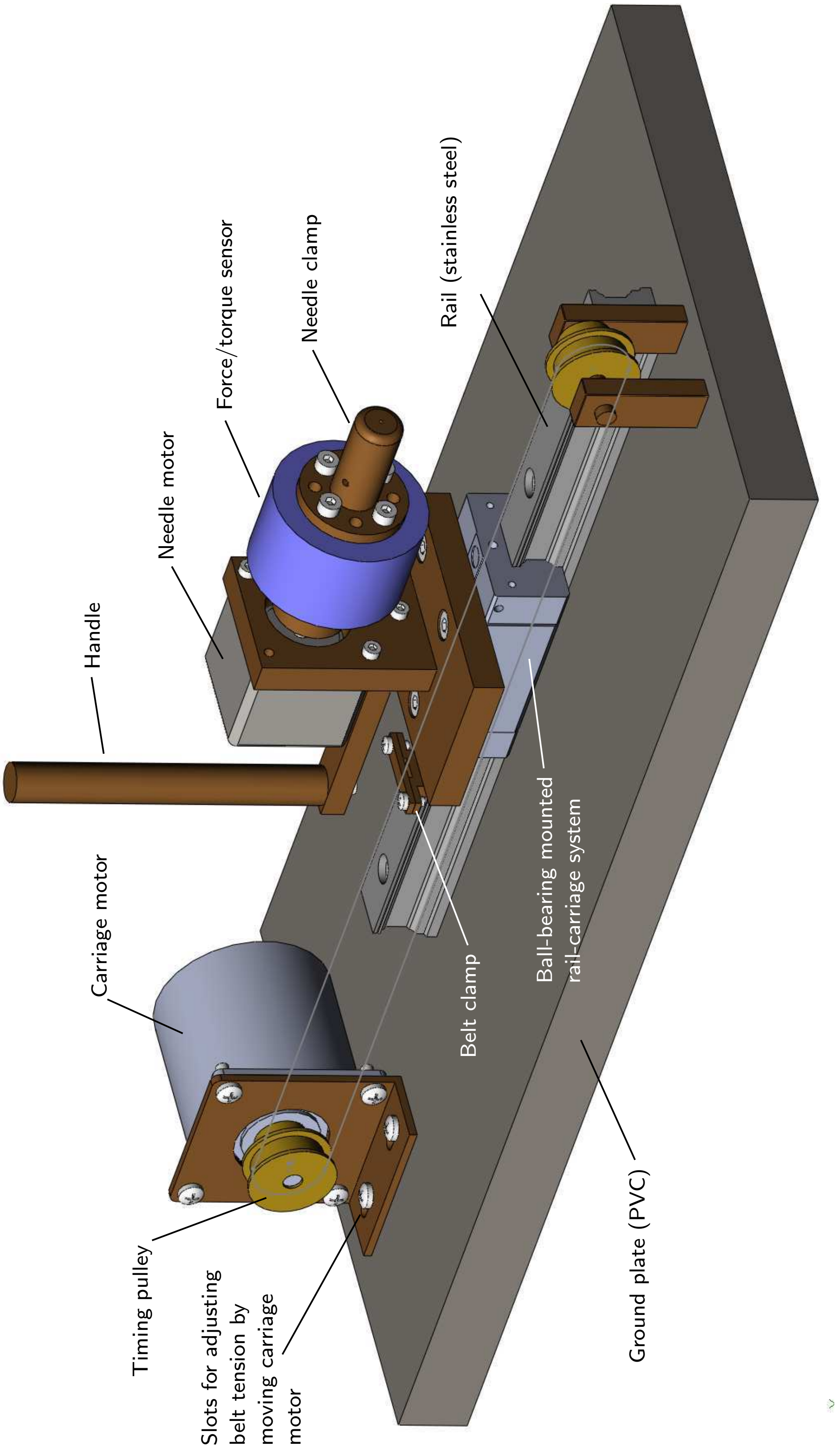

Figure A.3.: The CAD model of the assistant system as seen from above right.

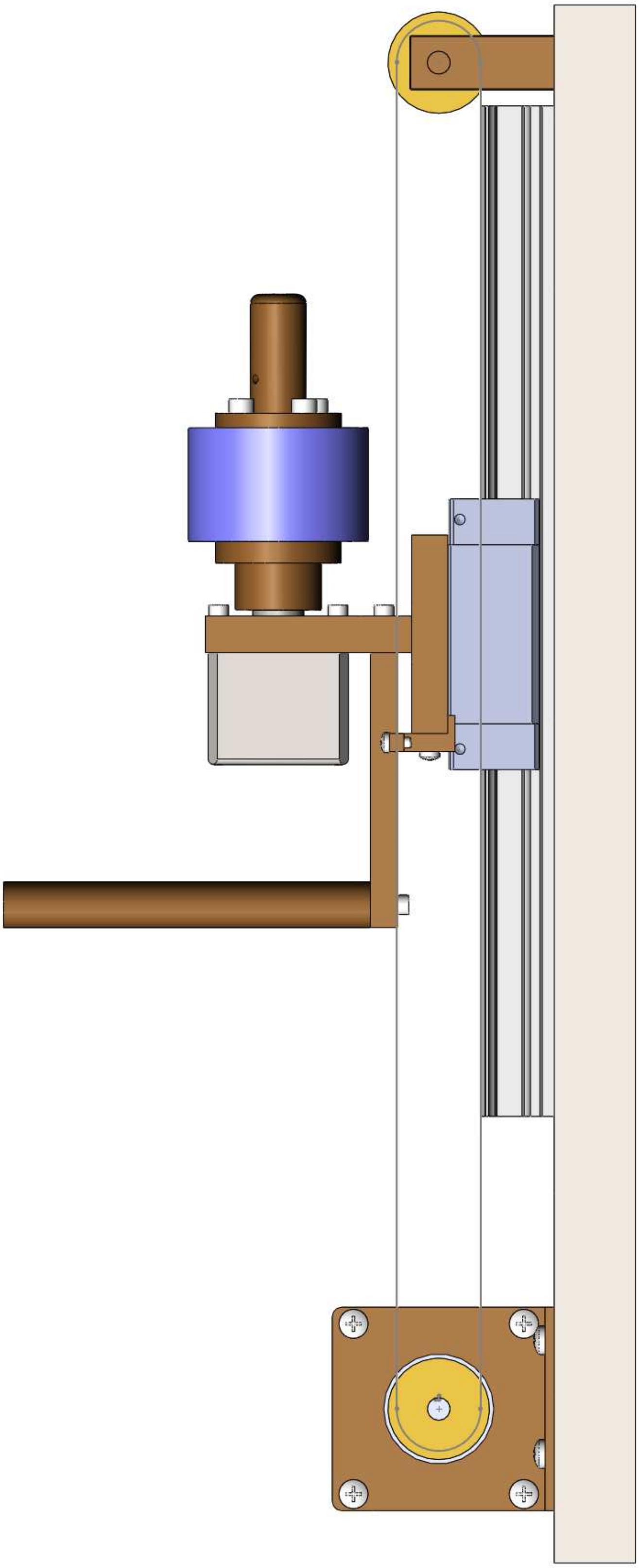

Figure A.4.: Right hand side view of the assistant system's CAD model.

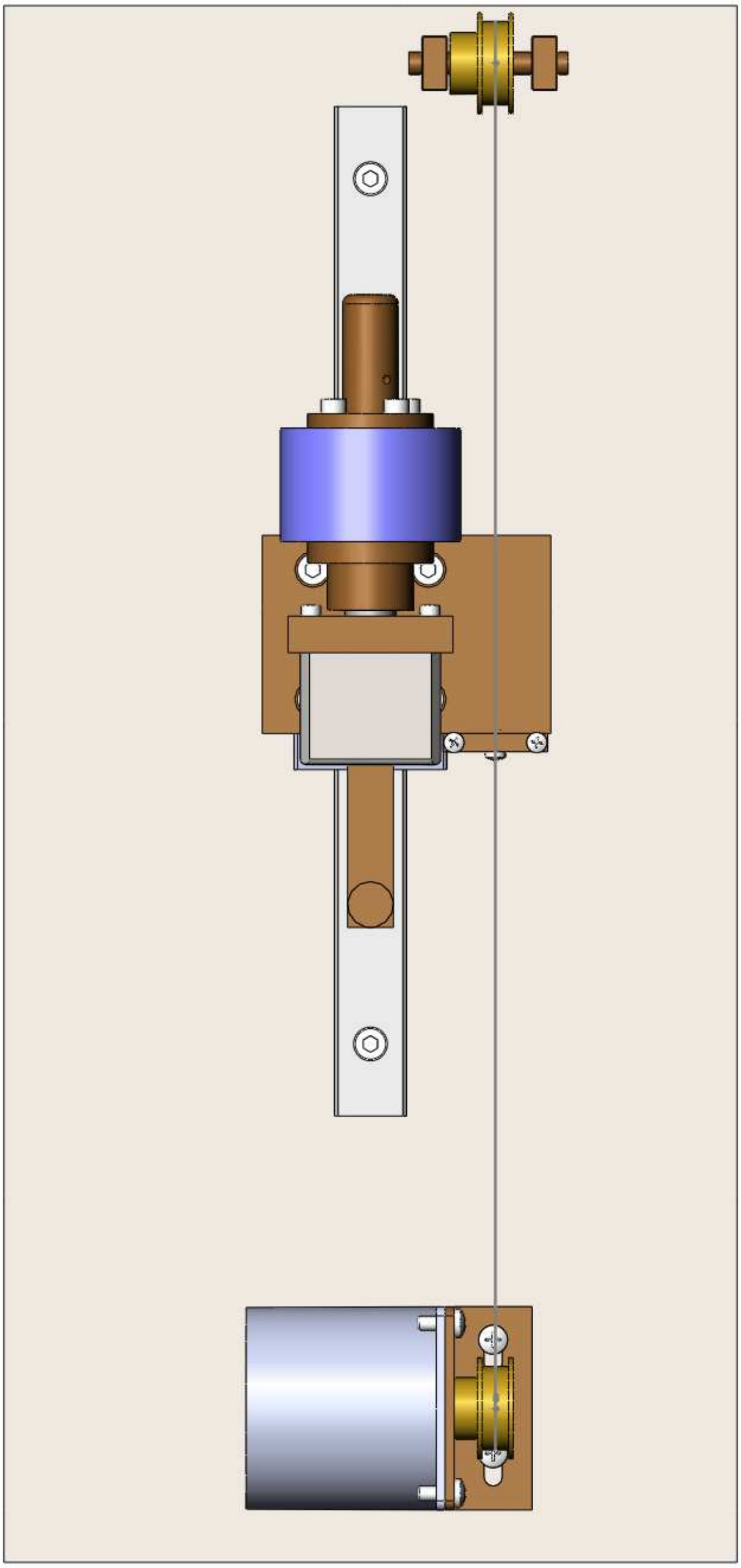

Figure A.5.: Top view of the assistant system's CAD model.

Appendix B.

Hardware

This chapter provides specific information about and instructions for the used hardware of the assistant system. Among the hardware components are the stepper motors, the HILINK data acquisition board and the force sensor.

B.1. Stepper Motors

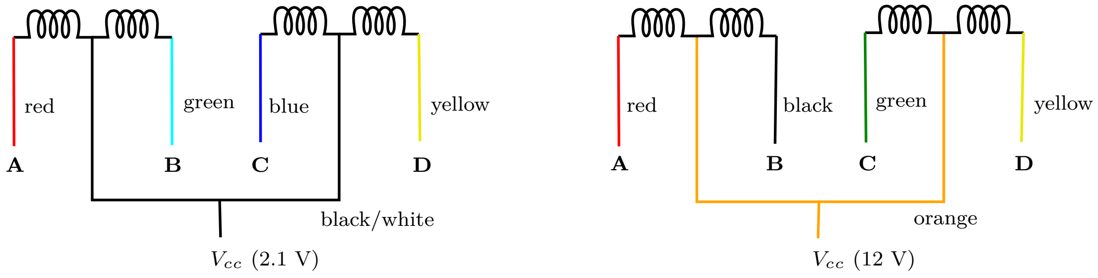

(a) Wiring layout of the carriage motor.

(b) Wiring layout of the needle motor.

Figure B.1.: Wiring for the stepper motors. **A**, **B**, **C** and **D** represent the connections to the controller.

Since the motors are salvaged parts from copiers or similar hardware, there were no data sheets available. Therefore, the wiring layout had to be found by measuring the resistance between each possible wire pairing for the case that the V_{cc} wires of each coil pairing are not connected to each other. Figure B.1 shows the wiring layout of each stepper motor. When the resistances of all wire pairings are compared, there should be three different resistance values. Pairings with highest resistance values indicate a connection for instance from **A** to **B** (cf. Figure B.1) and resistances of half the maximum value indicate a connection for instance from **A** to V_{cc}. The third resistance value is infinity or no connection, which is the case e.g. for pairing **B** and **C**. The order of the pairings, e.g. which wire identifies as **A**, which as **B** and so on, had to be found by trial and error.

The supply voltage (V_{cc}) for the needle motor is $12V$ and for the carriage motor $2.1V$ as indicated in Figure B.1. Although, to increase the torque of the carriage motor, the supply voltage can be increased to approximately $5V$ without damaging the motor. The motor should, however, not be connected to the power supply for an extended period of time in order to prevent overheating. It is also necessary to adjust the supply voltage of the carriage motor to approximately $4V$ to $5V$ for it to provide enough torque for needle insertion.

B.2. HILINK Real-Time Hardware-In-The-Loop Control Platform

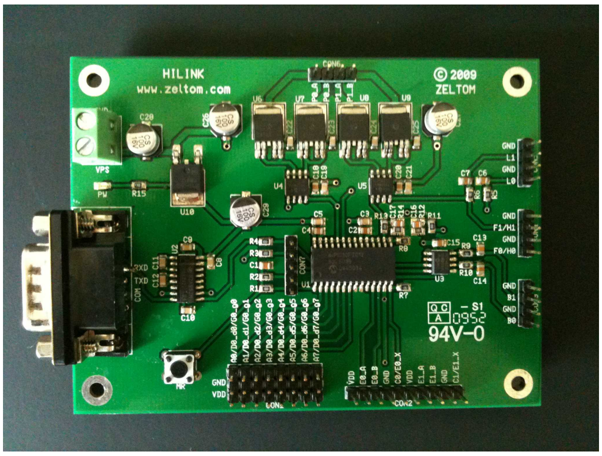

Figure B.2.: The HILINK data acquisition card [7].

The HILINK platform consists of the real-time control board and a Matlab/Simulink interface. The board has 8 analogue and digital ports, which can be used as both inputs and outputs. It provides 8×12 bit analogue inputs, 2×16 bit capture inputs, 2×16 bit encoder inputs, 1×8 bit digital input, 2×12 bit analogue outputs, 2×16 bit frequency outputs, 2×16 bit pulse outputs and 1×8 bit digital output. It also contains 2 H-bridges with 5A capability to drive external heavy loads.

The board comes with Simulink library blocks in order to establish communication. The HILINK library contains all necessary blocks for the in- and outputs of the hardware.

B.3. JR3 Force Sensor

The used force sensor of type *50M31A-I25* is manufactured by JR3 Inc. The outer dimensions of the sensor are 50 mm of diameter and 31 mm of thickness. The diameter of the bolt circle for the interfaces on both sides is 25 mm.

Figure B.3.: The JR3 force sensor.

The maximally admissible forces are 100N, 100N and 200N for the x-, y- and z-axis and maximum torques are 5 Nm for all three axes. The sensor's ADC has a resolution of 14 bits. Hence, the force resolution is 0.0061N, 0.0061N and 0,013N for the x-, y- and z-axis and the torque resolution is 0.0003Nm for all three axes.

The sensor is interfaced to a PC via a DSP based PCI receiver card. To program the sensor and read force/torque data, a C API is used. The API includes a static library and header file.

Appendix C.

Software

In this chapter, specifics about the used software of the assistant system is provided. The necessary code to communicate with and acquire data from the force sensor, the Simulink models and a Simulink library to control the assistant system are included.

C.1. Force Sensor S-Function Source Code

Listing C.1 and Listing C.2 contain the code snippets for initializing the force sensor and reading one data sample from the sensor as used in the Simulink S-Function blocks, which reads the JR3 sensor data. The code snippets are included in the functions *mdlStart()* and *mdlOutputs()* of the C S-Function source code.

Initializing the sensor involves waiting for initially occurring errors to clear, resetting the sensor offsets for all axes and calculating the sensor scales. For reading data samples, it is necessary to create the appropriate data structure which is compatible with Simulink (see lines 1-2 of Listing C.2) followed by acquiring the data from the sensor, scaling the data and assigning it to the Simulink data structure (see lines 6-11).

Listing C.1: The C code to initialize the force sensor.

```c
init_jr3(0x1762,0x3112,1,2,1,1);  //Input Values: vendor_ID, device_ID,
                                  //number_of_board, number_of_processors, download
while (read_jr3(ERRORS,0,1) != 0); //wait for errors to go away

reset_offsets(0,1);
use_offset(0,0,1);
delay(2000); //Give time to reset offsets

//Calculate the scales of the sensor ((1/2^14)*full_scale)
g_scaleF[0] = 1./16384 * 100;  //16384 = 2^14
g_scaleF[1] = 1./16384 * 100;
g_scaleF[2] = 1./16384 * 200;
g_scaleM[0] = 1./16384 * 5;
g_scaleM[1] = 1./16384 * 5;
g_scaleM[2] = 1./16384 * 5;
```

Listing C.2: The C code to read force and torque data from the force sensor.

```
real_T *fN = ssGetOutputPortRealSignal(S, 0);
real_T *mNm = ssGetOutputPortRealSignal(S, 1);

g_ft0 = read_ftdata(FILTER3,0,1);

fN[0] = (real_T)g_scaleF[0] * g_ft0.fx; //scaling force measurements from sensor 0
fN[1] = (real_T)g_scaleF[1] * g_ft0.fy;
fN[2] = (real_T)g_scaleF[2] * g_ft0.fz;
mNm[0] = (real_T)g_scaleM[0] * g_ft0.mx;
mNm[1] = (real_T)g_scaleM[1] * g_ft0.my;
mNm[2] = (real_T)g_scaleM[2] * g_ft0.mz;
```

C.2. Simulink Models

Figure C.2 shows the necessary blocks for controlling the assistant system. Some of the blocks are used in the Simulink models of Figure C.1 and Figure C.3.

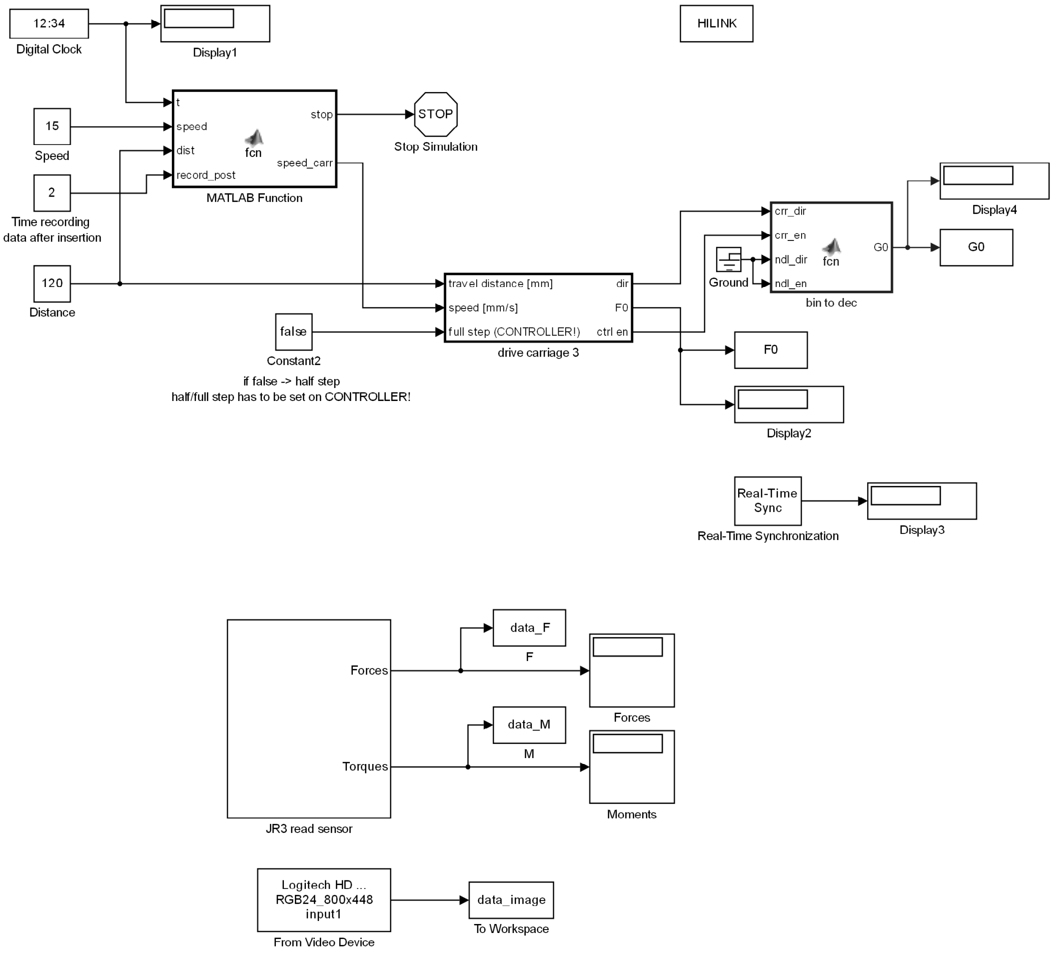

Figure C.1.: The Simulink model for needle insertion and simultaneous data recording.

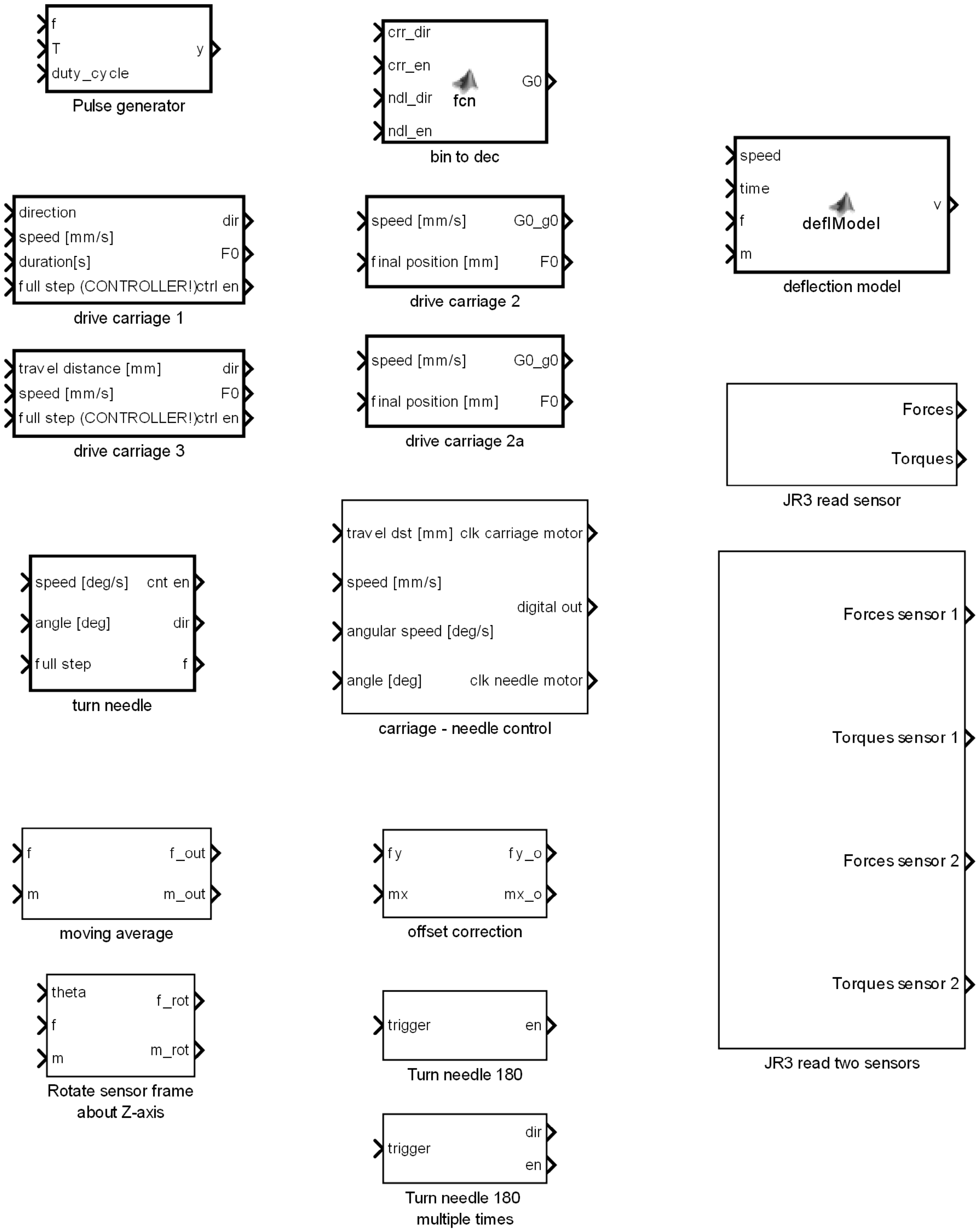

Figure C.2.: The Simulink library containing the blocks necessary for controlling the assistant system.

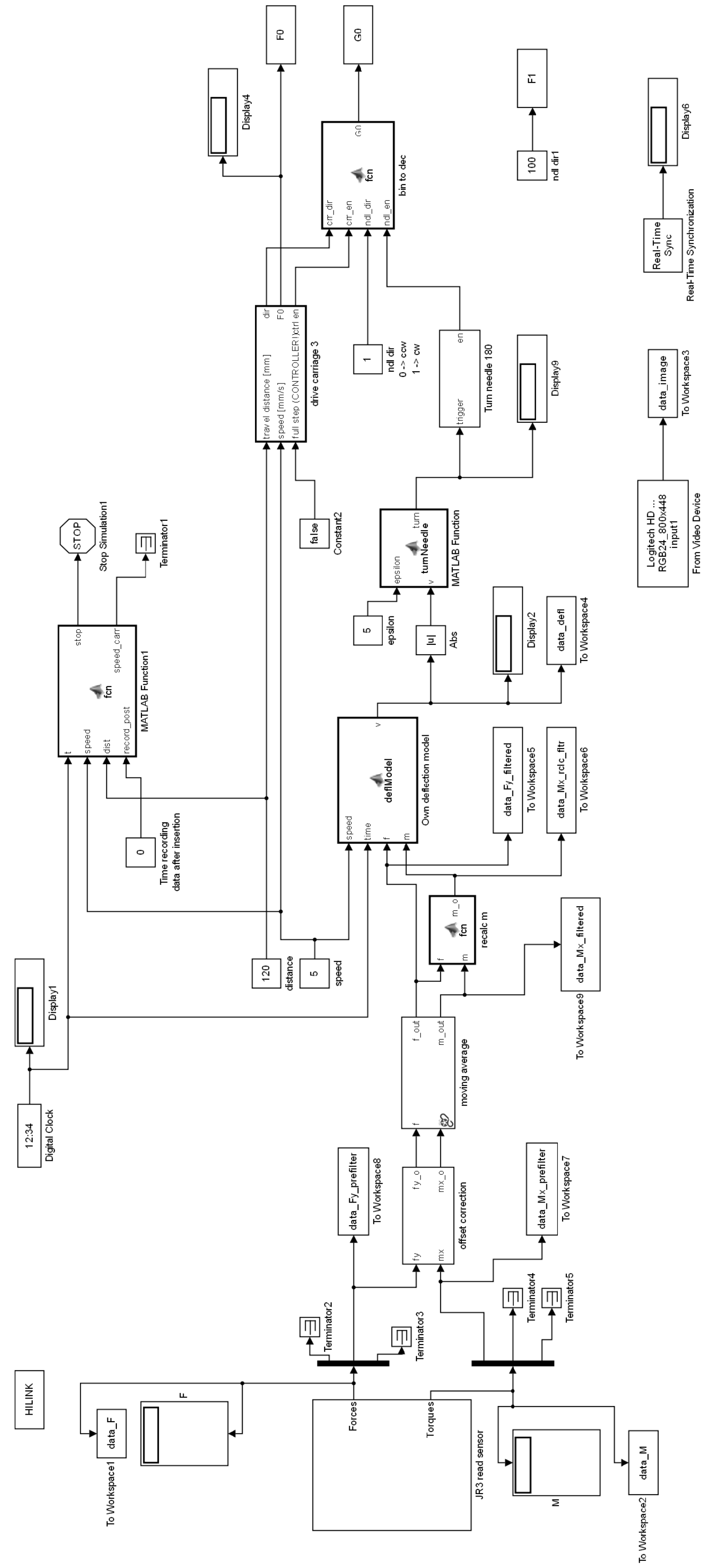

Figure C.3.: The Simulink model for needle insertion, simultaneous data recording, online deflection estimation and needle rotation.